

Solar Wind Turbulence

A Study of Corotating Interaction Regions at 1 AU

Jeffrey A. Tessein
Department of Physics
University of New Hampshire
Durham, NH 03824

May 15, 2009

Abstract

The solar wind is a supersonic flow of plasma coming out of the Sun and propagating throughout the heliosphere. Because of the Sun's rotation and the variability in the source of the solar wind, fast moving wind can crash into slow wind. This results in an interface that can repeat as the Sun rotates, known as a Corotating Interaction Region (CIR), where the slippage of fast wind past slow wind is a source of turbulence. I have taken 5 CIR events from the solar minimum years 2007 and 2008 to analyze their turbulence parameters and compared them to non-CIR (ambient) turbulence from solar maximum years. The CIR turbulence differs from the ambient turbulence because it is effectively a point source and the hope is to find evidence of turbulent energy emanating from the interface. This should present some nonhomogeneities not seen by non-CIR turbulence. We find that there are some differences with the CIR turbulence, but for the most part the CIR turbulence has the same results as past turbulence studies. This most likely means that the evolution of solar wind turbulence is faster than that of the source.

Contents

1	Basics of the Solar Wind	2
1.1	Properties of the Solar Wind	2
1.1.1	Magnetosphere	2
1.1.2	Termination Shock	3
1.2	History of Solar Wind Measurements	3
1.2.1	Current Missions	4
1.3	Solar Cycle	4
1.4	Coronal Mass Ejections	4
1.5	Origin of the Solar Wind	5
1.5.1	Parker Solutions	5
1.5.2	Three Mathematical Approaches to the Solar Wind	5
1.5.3	Solar Wind Development	7
2	Bulk Solar Wind at 1 AU	8
2.1	Fast And Slow Wind	8
2.2	Transients in the Solar Wind	8
2.2.1	Shocks	10
2.2.2	Corotating Interaction Regions	10
2.2.3	Magnetic Clouds	11
2.3	Cosmic Rays	11
2.4	Plasma	13
2.4.1	Magnetohydrodynamics	13
2.4.2	Plasma Waves	13
3	Fluctuations	16
3.1	Development of turbulence	16
3.2	Spectral Index	17
3.3	Geometry	17
3.4	Inertial Range	19
3.5	Dissipation Range	19
3.6	Helios Observations	20
3.7	Differences Between Fast and Slow Wind	21
3.8	Smaller Scale Analyses	21
4	Tessein Hourly Analysis	30
4.1	Background	30
4.2	Data Analysis	30
4.2.1	ACE 64 s Merged Data	31

4.2.2	ACE High Resolution MAG Data Analysis	37
4.2.3	Helios 1 MAG Data	38
4.3	Conclusions	39
5	Corotating Interaction Regions at 1 AU	40
5.1	Motivation	40
5.2	Data	42
5.3	Results	42
6	Discussion	52

Acknowledgements:

First and foremost, I would like to thank my advisor, Dr. Charles W. Smith, without whom none of this would be possible. I have come a long way from the first year physics major I was several years ago. Working for Dr. Smith has opened many doors for me, including publications, attending meetings, and acceptance to graduate school. The career path that lays ahead of me has been made possible by his excellent mentoring.

I would like to thank my fellow physics majors who have been excellent support over the last four years. Instead of being in constant competition with one another, my class has been more like a supportive community, of which being a member has been a pleasant experience.

I would also like to thank Dr. Bernie Vasquez for helping out with some important things.

Lastly, I need to thank my family and friends. They are good people and have always been there for me.

Chapter 1

Basics of the Solar Wind

1.1 Properties of the Solar Wind

The solar wind is a supersonic gas propagating throughout interplanetary space. It is an extension of the solar atmosphere driven by the difference in gas pressure between the Sun and space. The vast majority of the constituent particles are protons and alpha particles (${}^4\text{He}^{2+}$). Helium also has an average abundance of 4-5% by number. In addition, isotopes up to Iron have been observed [16]. The solar wind has an average density of about 10 cm^{-3} near Earth. Density is dependent on solar activity and wind speed; during times of solar activity the density tends to spike. Wind speed can vary from 200 km/s to 1000 km/s, however, nominal speed during times of reduced solar activity is 400 km/s to 600 km/s. The average temperature is about 10^5 K , although at such an extremely low density, there is very little heat capacity. Like density, the temperature is related to solar activity.

Just as with Earth, the Sun has a mostly dipolar magnetic field. The process that generates the magnetic field is called a dynamo. It is suspected that the magnetic field is generated by rotating charged fluid in the interior. The solar magnetic field encompasses the entire solar system and is known as the Interplanetary Magnetic Field (hereafter referred to as the IMF).

The IMF is coupled to the solar wind and is carried out by it. Local electromagnetic interactions are governed by the geometry of the IMF. Ions gyrate around the field lines. The gyration has a characteristic radius given by

$$r = \frac{mv_{\perp}}{|B|} \quad (1.1)$$

1.1.1 Magnetosphere

When the solar wind reaches a planet with a magnetic field, like Earth, it interacts. Earth's magnetic field generates a barrier around the planet, known as the magnetosphere. On the day side of the magnetosphere and around part of the night side, there exists an interface known as the bow shock. This is the location where the ram pressure of the solar wind equilibrates with the magnetic pressure of Earth's magnetosphere. This effect is similar to a rock in a fast moving river. There is a stationary shock wave in the stream that causes the water to slide around the rock. In the case of the magnetopause, the shock does move depending on the pressure from solar wind (for example, a solar storm can compress the bow shock closer to Earth). Likewise, during quiet solar wind, Earth's magnetic field is

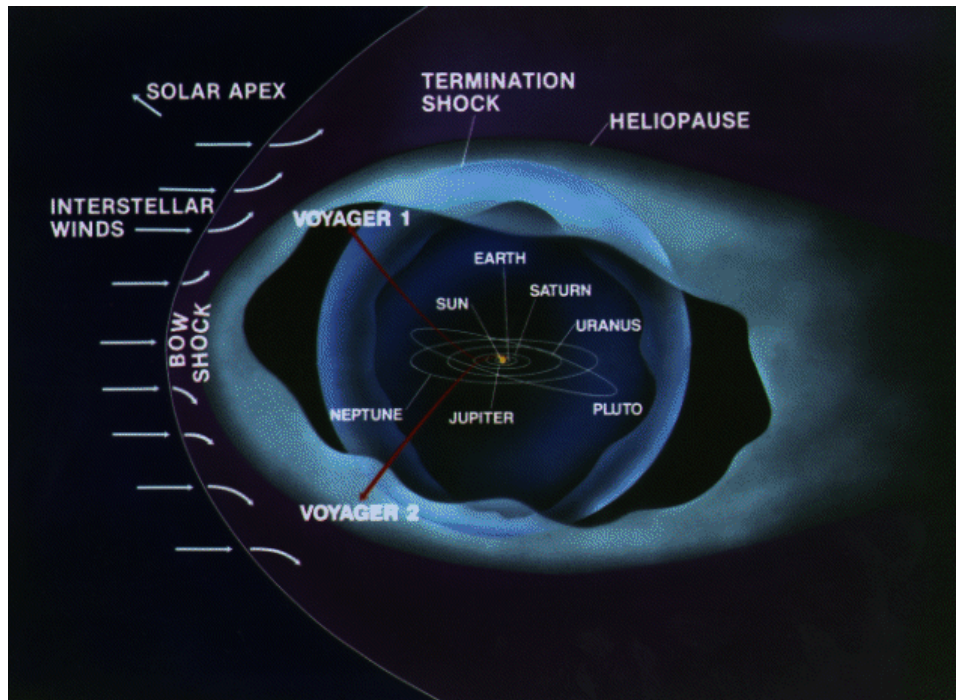


Figure 1.1: Artist's rendition of the heliosphere. (*Image courtesy of NASA*).

able to push the bow shock sunward. As the solar wind is diverted around the side of the magnetosphere, it forms a long, narrowing boundary on the night side of Earth, called the magnetotail.

1.1.2 Termination Shock

The solar wind extends out to approximately 100 AU (1 AU is equivalent to the Earth-Sun distance) where it reaches the termination shock. This is the point where pressure from the solar wind balances with the Local Interstellar Medium (LISM). When the solar wind reaches the heliopause, it joins with the flow of the LISM. The termination shock completely surrounds the heliosphere and is approximately bullet shaped. The shock has become an object of study in recent years because we are getting our first in situ measurements of it from Voyagers 1 and 2. An artists depiction of the entire heliosphere is shown in Figure 1.1.

1.2 History of Solar Wind Measurements

Studies of solar-terrestrial relations have a long history. Before the space age there were numerous ways to remotely measure the effects of solar activity on our planet. Aurora studies go back thousands of years, and chemical analysis of tree rings is also an indicator of the sunspot record (sunspot number correlates to solar activity). A lack of solar activity from 1645 to 1715, called the Maunder Minimum, has been linked to unusually cold weather. Viking settlements in Greenland correspond to what is known as the Medieval Warm Period immediately preceding the Maunder Minimum. During the Maunder Minimum, Vikings abandoned Greenland, possibly due to climate change. In the twentieth century, studies of comet tails portended the existence of a solar wind. Astronomers found that comets contain a

second tail that always points anti-sunward. In addition to a dusty tail, a comet has a second tail that contains ions. This is known as a plasma tail. The observation that the plasma tail always points anti-sunward meant that there must be a continuous solar wind. During the early 1950s most astronomers thought that the solar wind only came in intermittent bubbles. It was referred to as solar corpuscular radiation. In 1958 Eugene Parker predicted the existence of a continuous, supersonic solar wind. This was soon confirmed by in situ measurements from early satellites. This forms the basis for our current picture of the solar wind.

1.2.1 Current Missions

The arrival of the space age has greatly increased our knowledge of the solar wind. In the 1970s the Helios spacecraft went within 0.3 AU of the Sun; the closest of any spacecraft to date. A new mission, Solar Probe, is scheduled to get much closer to the Sun around 2015. The two Voyager spacecraft, launched in 1977, have reached the termination shock and are returning the first in situ measurements of the boundary regions between the Heliosphere and the LISM. As of 2009, the IBEX mission is mapping the termination shock by measuring neutral particles coming in from the LISM. Ulysses, launched in 1990, did several polar orbits about the Sun, revealing much about properties of the high-latitude solar wind. The spacecraft that will be used for this thesis, ACE (Advanced Composition Explorer), was launched in 1997 and takes plasma measurements at the L1 point between the Sun and Earth.

1.3 Solar Cycle

The Sun goes through eleven year cycles of activity, switching between stages of solar minimum and solar maximum. This effect is thought to be a result of the Sun's differential rotation. Because the Sun is not a rigid body, its equatorial regions rotate faster than the polar regions. Because low latitudes on the Sun rotate faster than high latitudes (the equator has a rotational period of about 25 days and the polar latitudes take about 29 days to complete a rotation), the magnetic field can quickly become twisted and mangled. It is thought that as the field becomes more and more distorted, there is an increase in solar activity. This is the rise toward solar maximum. Eventually, when the field becomes extremely distorted it is able to reset itself, and the process begins again. At this point, the Sun would be returning to solar minimum. The details of the resetting process are mostly unknown. During the time that the magnetic field is highly distorted the sunspot count becomes elevated; likewise, when the Sun's magnetic field is more dipolar the sunspot count is low. The last solar maximum was around 2001, and as of 2009, the Sun is coming out of solar minimum into the next maximum. It is during the solar maximums that we see the most solar flares and CMEs (see Section 1.4), which can occur several times a week. During solar minimum these phenomena are only seen a few times a year, and tend to be smaller in magnitude.

1.4 Coronal Mass Ejections

Sometimes magnetic energy on the Sun can cause a violent release of energy, eventually triggering a Coronal Mass Ejection (CME). The CME begins as a prominence. A prominence

is a magnetic field line coming off the surface of the Sun and going back in, forming a loop of plasma emitting visible light. The footprints of the prominence are areas of opposite magnetic polarity. At some point the prominence builds up enough energy to release massive amounts of matter. This is thought to be a result of magnetic reconnection; a process where magnetic field lines cross, disconnect, then reconnect with a new topology, releasing energy. In a typical CME, a massive amount of matter is released from the Sun in one giant burst. This release of energy triggers extremely hot and fast solar wind, and because of the supersonic speeds, a shock. When the CME reaches Earth it interacts with the day side of the magnetopause. The interaction sends current around to the night side of the magnetosphere and upon reaching it, connects to the ionosphere. Upon reaching the ionosphere a geomagnetic storm is triggered. The visible result of geomagnetic storms are auroras, however there are other effects as well. A geomagnetic storm can cause current to run through power lines damaging them, and can throw off GPS signals and radio communication. One little known impact of geomagnetic storms is on racing pigeons. Since the pigeons use the geomagnetic field as a guidance system, they lose their sense of direction during a geomagnetic storm. During solar activity the Space Weather Prediction Center in Boulder, Colorado warns pigeon racers to cancel any events that they have planned until the geomagnetic field settles. CMEs are also often seen at the same time as solar flares, which are an intense release of radiation from the Sun. This source of extreme solar activity is coronal holes. A coronal hole is a structure on the Sun that acts as a source of hot, fast solar wind. It is not really a hole in the corona; rather a coronal hole is an area of lower density plasma in the solar atmosphere. The coronal holes tend to appear during times of increased solar activity and are associated with flares and CMEs. At high solar latitudes there are permanent coronal holes. High speed solar wind (often coming from coronal holes), $V_{SW} > 500$ km/s, is fundamentally different from low speed solar wind, $V_{SW} < 400$ km/s. High speed streams are hotter and more tenuous, while low speed winds have a higher density and are not as hot.

1.5 Origin of the Solar Wind

1.5.1 Parker Solutions

In his landmark 1958 publication, Eugene Parker unveiled his hydrodynamic approach to the solar wind [25]. In this publication Parker predicted that the hydrostatic model of the corona, the leading theory of the time, was unphysical. Parker applied Bernoulli's equations and came up with several branches of solutions to the differential equations [26]. These are shown in Figure 1.2. Plotted on the x-axis is distance from the Sun while the y-axis is solar wind speed. The critical point in the middle is the speed of sound for Alfvén waves. Solutions E and D are unphysical and solutions B and C do not match observations. The F branch is known as the “solar breeze”. Parker was able to determine that solution A is the one representing the solar wind and that it is supersonic. This led to the theory of the hydrodynamic corona. Parker's predictions were confirmed by the first in situ observations a few years later.

1.5.2 Three Mathematical Approaches to the Solar Wind

The solar wind can now be described at different levels of complexity. The first level of abstraction is the purely kinetic particle approach. In this approach we look at the solar

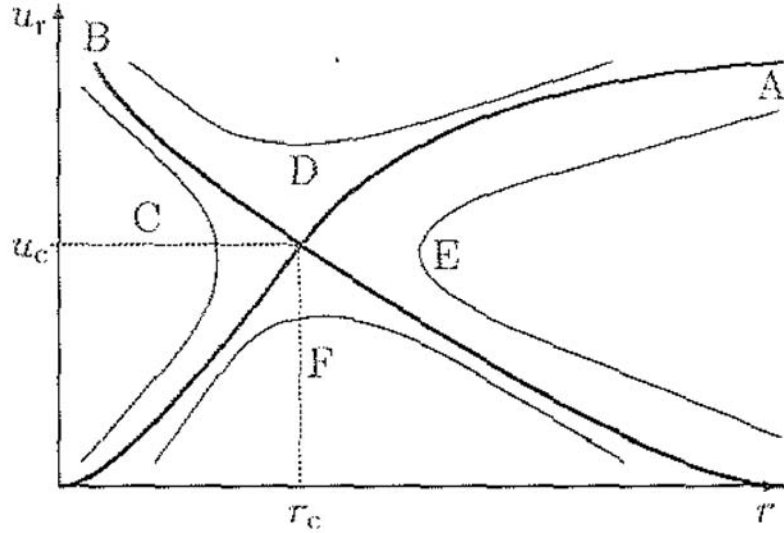


Figure 1.2: The Parker solutions[17]

wind as a collection of individual particles. In principle every charged particle sees every other charged particle (ignoring Debye shielding for the moment). This means that the total force F_i on any particle i is the sum of all electric and magnetic forces from all other particles:

$$F_i = \sum_j [(F_E)_{i,j} + (F_M)_{i,j}] \quad (1.2)$$

where

$$(F_E)_{i,j} = q_i q_j / r_{i,j}^2 \quad (1.3)$$

is the electric force on a particle i from particle j and

$$(F_M)_{i,j} = q_i \mathbf{v}_i \times \mathbf{B}_j \quad (1.4)$$

where \mathbf{B}_j is the magnetic field from particle j and F_M is the magnetic force. The energy, velocity, charge, mass, etc. of each particle is taken into account. This method is the most precise but can get very complicated.

The second level of abstraction is the Vlasov Equation:

$$\frac{\partial f}{\partial t} + \mathbf{v} \cdot \nabla f + \frac{q}{m} (\mathbf{E} + \frac{\mathbf{v} \times \mathbf{B}}{c}) \cdot \frac{\partial f}{\partial \mathbf{v}} = 0 \quad (1.5)$$

where f is particle density in six dimensional phase space, \mathbf{v} is velocity, q is charge, and m is mass. To this we add Maxwell's equations to evolve the electromagnetic fields. This focuses on an ensemble of particles and distinguishes each particle type.

The third level of abstraction is magnetohydrodynamics (MHD). This approach treats the solar wind as a magnetized fluid. MHD is described by the induction equation (1.14) which can be derived from Amperè's Law.

$$\nabla \times \mathbf{B} = \mu_0 \mathbf{j} + \frac{1}{c^2} \frac{\partial \mathbf{E}}{\partial t} \quad (1.6)$$

In the nonrelativistic limit, $\frac{1}{c^2} \frac{\partial E}{\partial t} \rightarrow 0$. Hence,

$$\nabla \times B = \mu_0 j \tag{1.7}$$

$$j = \sigma(E + \vec{v} \times B) = \frac{\nabla \times B}{\mu_0} \tag{1.8}$$

$$E = -\vec{v} \times B + \frac{j}{\sigma} \tag{1.9}$$

Let $\eta = \frac{1}{\mu_0 \sigma}$. Then we apply Faraday's Law of Induction.

$$\nabla \times E = -\frac{\partial B}{\partial t} \tag{1.10}$$

$$\frac{\partial B}{\partial t} = -\nabla \times \left(-\vec{v} \times B + \frac{j}{\sigma} \right) \tag{1.11}$$

$$\frac{\partial B}{\partial t} = \nabla \times (\vec{v} \times B) - \nabla \times \eta (\nabla \times B) \tag{1.12}$$

$$\nabla \times (\nabla \times B) = \nabla(\nabla \cdot B) - (\nabla \cdot \nabla)B \tag{1.13}$$

This brings us to the MHD Induction Equation.

$$\frac{\partial B}{\partial t} = \nabla \times (\vec{v} \times B) - \eta \nabla^2 B \tag{1.14}$$

The first term describes the changes in the magnetic field from plasma oscillations and is called the convection term. The second term is the resistive term. In the infinite conductivity limit ($\eta \rightarrow 0$) we can eliminate the second term. This is the limit in which the frozen-in condition applies. The frozen in condition states that as the plasma propagates and changes its shape, the flux will not change. This means that in the reference frame of a parcel of solar wind the magnetic field topology is unchanging. To this we add the Navier-Stokes equation, which describes the evolution of a fluid. Magnetic terms derived from the Vlasov-Maxwell equations are added to the Navier-Stokes equation.

1.5.3 Solar Wind Development

The Sun rotates with an average period of about 27 days (recall that the rotation is differential and dependent on latitude). This causes the magnetic field coming off the Sun to be wound in the shape of an archimedian spiral. This also affects the solar wind parcels coming off the Sun. The effect is much like a water sprinkler releasing water while spinning. The water still moves radially but has a tangential component to its motion. In this same way, the power in the solar wind propagates radially. This winding of the magnetic field leads to the shape of what we know as the Heliospheric Current Sheet (HCS), the neutral plane of the Sun's magnetic field. The shape of the HCS is often described as a "ballerina skirt". It becomes more wavy, and exhibits larger disturbances in amplitude during solar maximum. During solar minimum, the shape of the HCS becomes more simplified.

All these properties affect the solar wind we measure at 1 AU. It is a magnetized fluid containing shocks, interface regions and turbulence. All the aspects of interplanetary space written about above contribute to the transient and turbulent properties of the solar wind discussed in Chapter 2.

Chapter 2

Bulk Solar Wind at 1 AU

2.1 Fast And Slow Wind

We see two different types of solar wind at 1 AU. As mentioned earlier, there is the hot, tenuous fast wind, and the cooler, more dense slow wind. The following plots come from a code I worked on from 2006 into 2008 (this code is explained further in Chapter 4). Figures 2.1 and 2.2 show this difference remarkably well. Also shown is β_P plotted against proton speed. β_P is the ratio of plasma pressure to magnetic pressure for the protons. If $\beta_P > 1$, the plasma is called ‘warm’ and if $\beta_P < 1$, the plasma is ‘cold’. In the solar wind, $0.1 < \beta_P < 1.0$. Figures 2.1, 2.2 and 2.3 all show standard solar wind properties discussed in Chapter 1. These figures were a nice test to see if the code was working. The scatter in each of these plots is exactly what one would expect from nominal solar wind.

2.2 Transients in the Solar Wind

The solar wind can be thought of as a continuous fluid periodically interrupted by what is known as transient events. These transients disturb the solar wind and do not exhibit nominal solar wind properties. Indeed, many solar wind studies exclude transients from their analyses.

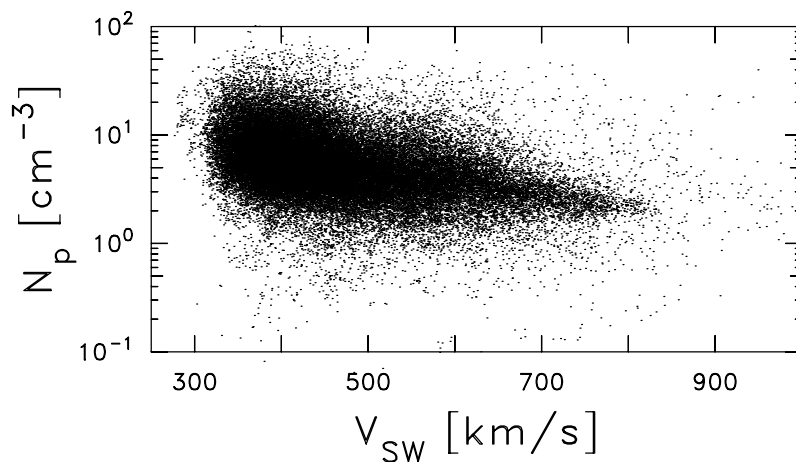


Figure 2.1: Proton density plotted against proton speed.

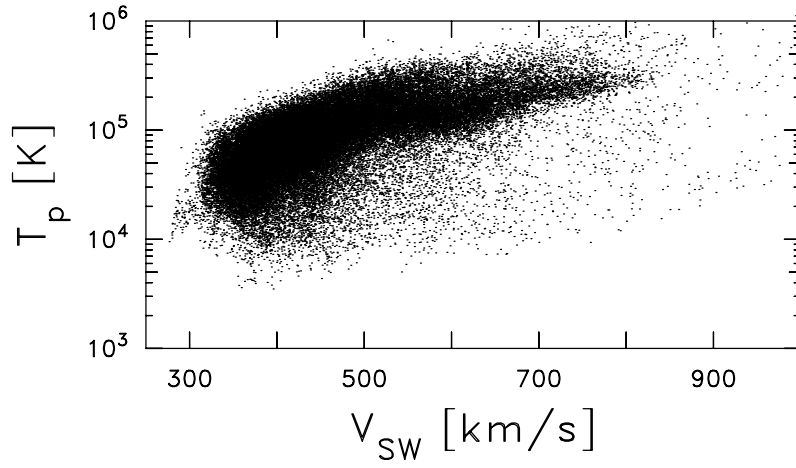


Figure 2.2: Proton temperature plotted against proton speed.

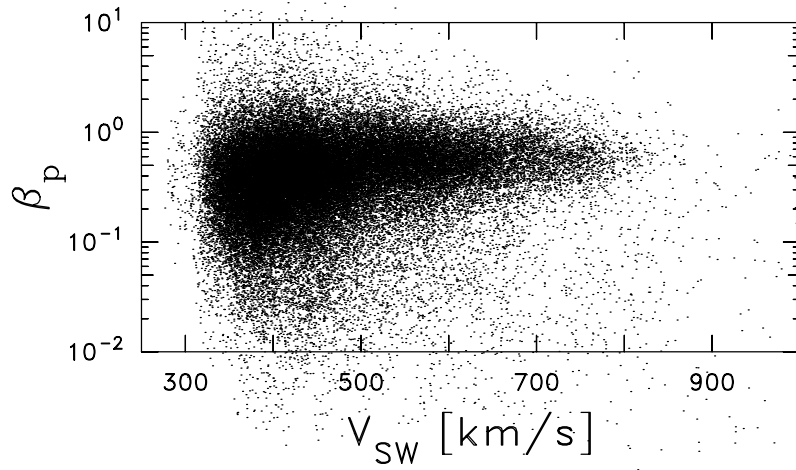


Figure 2.3: Plasma β_P is the ratio of plasma pressure to magnetic pressure. β_P appears to converge at higher V_{SW} .

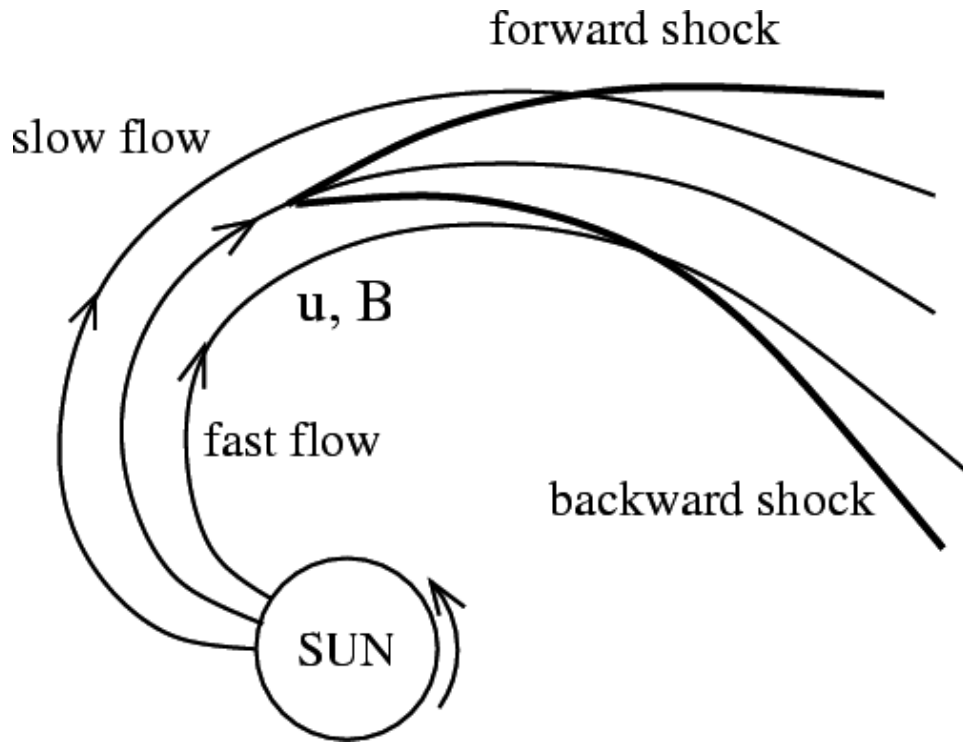


Figure 2.4: Schematic of a CIR [13]

2.2.1 Shocks

One major transient in the solar wind is a shock. Shocks have already been mentioned in the discussion of bow shocks. Bow shocks are known as standing shocks because they are stationary in the frame of a magnetosphere. However, shocks do propagate. A moving shock is generated by a source moving faster than the signal speed of the medium. In plasma physics a shock is important because it represents a boundary between two different mediums. The shocks that we are familiar with, such as sonic booms, are known as gas dynamic shocks. Gas dynamic shocks transfer information through particle collisions. In space plasmas, the density is low and collisions are very rare (the mean free path is around 1 AU). This results in collisionless shocks. Collisionless shocks are able to transfer information through electromagnetic interactions rather than collisions. This is very similar to the concept of magnetic pressure and tension in MHD. Pressure and tension, processes normally thought to occur with collisions, occur without collisions because the magnetic field has the same effect. Behind the shock there is a transition back to the medium of the foreshock (the region ahead of the shock). If the transition is fast, a reverse shock can occur.

2.2.2 Corotating Interaction Regions

As the Sun rotates, there is variability in the solar wind it emits. This variability is most pronounced at low latitudes. As a result of the variability and rotation, fast solar wind can “catch up” to slow solar wind. This results in an interface region, and creates a transient in the solar wind known as a Corotating Interaction Region (CIR). Figure 2.4 shows a schematic of a CIR.

A CIR can easily be identified by the discontinuities it creates in the solar wind. At

the interface, electron temperature rises and alpha particle abundance increases [29]. Radial evolution of the CIR leads to a steepening of the velocity gradient at the interface; if this becomes sufficiently steep a shock will form [29]. Upstream of the interface is a spike in proton density and temperature. A common feature of the fast-to-slow interface is an increase in the Mg/O ratio [29].

Flow velocity is in opposite directions, always away from the interface. As a result, a shock can propagate in both directions away from the interface. This is known as a forward/reverse shock pair. When a CIR occurs, there is a compression region at the interface where magnetic field lines come together. Magnetic structures do not merge together because they are “frozen in” to the solar wind and the field lines do not cross [29].

Because the solar variability that causes CIRs is mostly limited to low latitudes on the Sun, CIRs are not seen as frequently at high solar latitude. However, higher latitude CIRs can occur as a result of the tilt of the Sun’s dipole, which is around 7° . Gosling and Pizzo found that at high latitudes, only reverse shocks were found [13]. The transition from forward/reverse shock pairs to only reverse shocks occurs at a latitude roughly equivalent to the tilt of the Sun’s magnetic dipole, and this tilt may be the reason for the effect.

2.2.3 Magnetic Clouds

Magnetic clouds were first defined by *Burlaga et al.* in 1981 [6] and an example of one is shown in Figure 2.6. A magnetic cloud is a configuration in the IMF in which there exists higher than average magnetic field strength and the field vectors rotate parallel to a plane. *Burlaga et al.* found that the frequency of occurrence of these depends on the solar cycle. The radius of a typical magnetic cloud at 1 AU is 0.25 AU, and is proportional to heliocentric distance. Clouds tend to expand with a speed of around 45 km/s and also have translational motion that is usually equivalent to the speed of the background solar wind. An example of magnetic cloud data is shown in Figure 2.5.

2.3 Cosmic Rays

A cosmic ray is a high energy charged particle moving through the plasma. It can come from the Sun, or from outside the heliosphere. Galactic Cosmic Rays (GCRs) come from outside the heliosphere and have enough energy to penetrate the interstellar bow shock. As a result, they are often travelling near the speed of light. These cosmic rays frequently reach Earth and make a significant contribution to the natural background radiation we experience. When cosmic rays reach Earth’s atmosphere, the particle will crash into it and break apart. This will generate new particles and gamma rays, which will also interact with the atmosphere. The gamma rays and particles that finally reach the ground can be traced back to their parent particles.

The cosmic rays described above are known as Galactic Cosmic Rays (GCRs). There are also Anomalous Cosmic Rays (ACRs). These are high energy particles that originated in the heliosphere and interacted with the termination shock before returning to the inner heliosphere. We know that this happens because they disrupt the nominal cosmic ray spectrum. Forbush showed that cosmic rays are modulated by solar activity. Cosmic ray flux at Earth increases and decreases with anti-correlation to the solar cycle. The decrease during solar maximum is known as the Forbush Decrease.

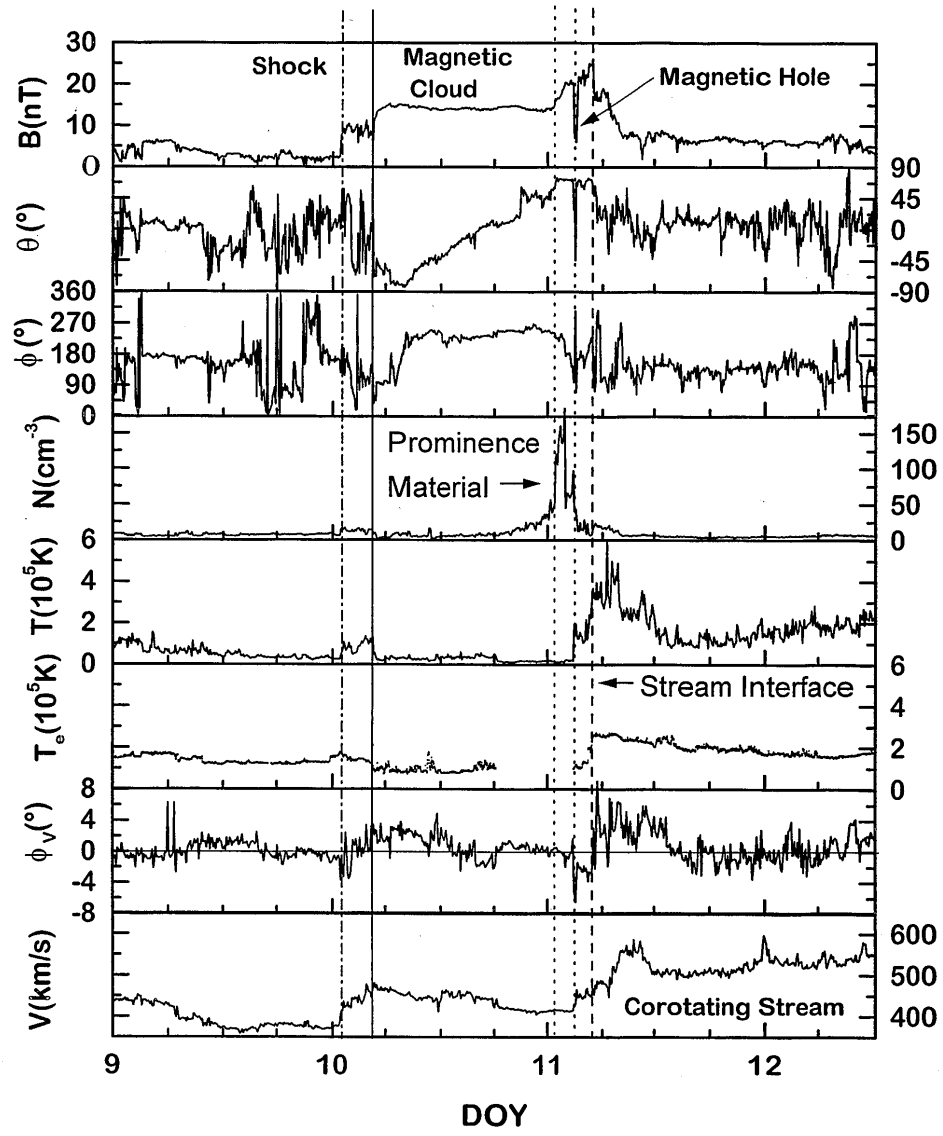


Figure 2.5: Magnetic cloud data [6].

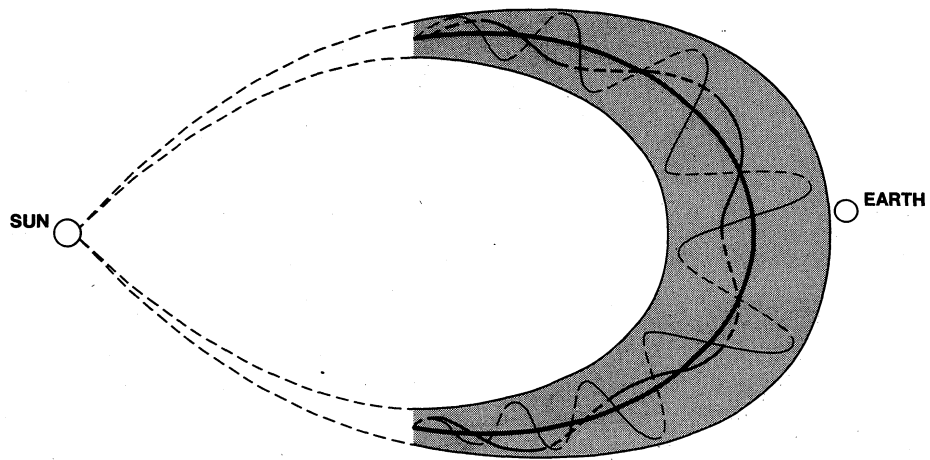


Figure 2.6: Large scale schematic of a magnetic cloud [6].

In addition to cosmic rays it is commonplace for neutral particles from the LISM to enter the heliosphere. In the vacuum of space, there are essentially no barriers to these neutral particles like there are for the ions.

2.4 Plasma

The constituent particles of the solar wind are at sufficiently high energies that all particles are disassociated from their molecular bonds. This is the main feature of a plasma. An important aspect of any plasma is the shielded potential. The shielded potential effect, known as Debye Shielding, is a result of a group of ions occupying the same area. In the frame of an ion in space, electromagnetic interactions will result in that ion pulling toward it ions of opposite charge. The oppositely charged ions pulled in will effectively shield the ion from other particles and reduce the effects of their forces to the point that electromagnetic interactions are eliminated outside of the Debye Shield. This spherical potential formed around the ion has a radius known as the Debye Length.

Another aspect of a plasma is plasma oscillations. Because of the magnetic fields that exist in the solar wind, the ions are constantly in motion. In a plasma, there exist domains that are dominated by one charge or another. This happens because the scattering of charges is not homogeneous. An oscillation can form as a result of an ion drifting into an area that is dominated by ions of the same charge. The coulomb repulsion will force the ion out of the domain. However, this ion will go too far and enter a different domain of like charge. The restoring force is the plasma trying to equilibrate the domains. When this happens to an ensemble of particles, plasma oscillations result.

2.4.1 Magnetohydrodynamics

One of the most useful ways to study a plasma is with Magnetohydrodynamics (MHD). Some MHD concepts important to the study of plasmas are magnetic pressure, magnetic tension, reconnection and flux tubes. Magnetic pressure is a result of energy density in a magnetic field and is defined by the equation $\frac{B^2}{2\mu_0}$. When magnetic field lines become compressed, they will eventually reach a point where they are so dense, they will resist any further forcing. An example of magnetic pressure is in Earth's magnetopause. Magnetic pressure there resists the ram pressure from the solar wind.

Magnetic tension is the rigidity of magnetic field lines. When a magnetic field line is perturbed it will oscillate then return to where it was. This effect is much like the plucking of a guitar string. A flux tube is formed by the gyrokinetic rotation of particles. As a particle travels down a magnetic field line, it rotates in a helical path with a characteristic radius. An ensemble of identical particles with the same radius form a tube. In a 2008 publication, Borovsky [5] states that interplanetary space is filled with flux tubes, like a bowl of spaghetti.

2.4.2 Plasma Waves

Central to the study of turbulence in the solar wind is plasma waves. A plasma wave is any type of disturbance that propagates through the plasma. As a plasma wave propagates, the fluctuating quantity can be any property of the solar wind, but is often limited to magnetic field and particle velocity. The plasma waves most important to solar wind study are Alfvén waves and magnetosonic waves.

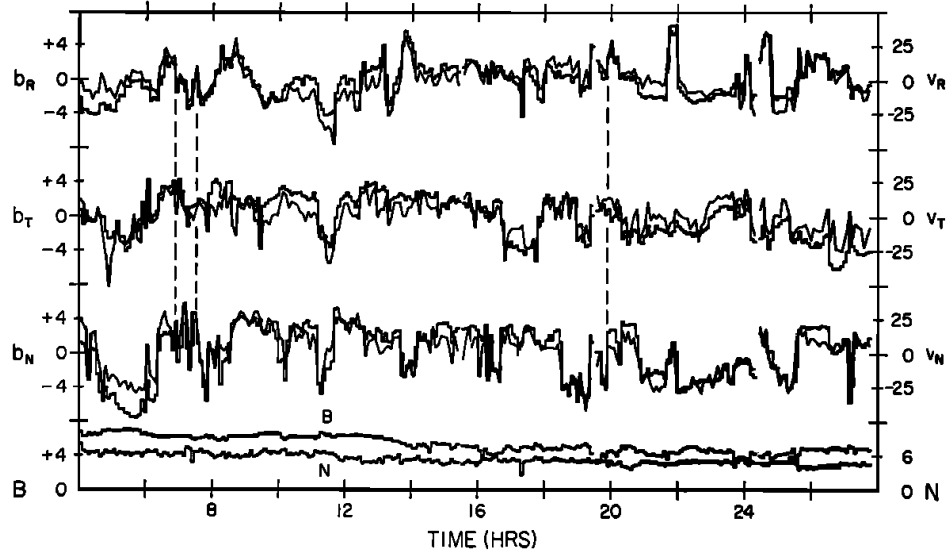


Figure 2.7: Alfvén waves. The magnetic field and velocity fluctuate together while the density remains constant[3].

An Alfvén wave propagates along a magnetic field line. It is similar to plucking a guitar string and sending a disturbance along the string. The restoring force is magnetic pressure and tension. When there is a transverse perturbation on the field line, magnetic tension restores the field line to where it was. In Figure 2.7, we can see Alfvén waves.

Magnetosonic waves have the same restoring force as Alfvén waves but propagate perpendicular to the field lines. These are longitudinal waves that compress the field lines, increasing the density. By compressing the field lines together, a magnetic field gradient is formed and the field lines return to where they were.

Belcher & Davis propose several theories for the origin of Alfvén waves [3]. One possibility is that they are produced by instabilities in the plasma. These instabilities can arise from expansion of the corona. Another theory is that they are produced locally in the solar wind. This would be a result of CIRs causing turbulence, which is the origin of the waves. One problem with this theory is that CIRs are not common enough to explain how many Alfvén Waves there are in the solar wind. A third theory is that these waves are remnants of processes occurring in the photosphere and chromosphere of the Sun. A problem with this theory is that Alfvén waves are more energetic than theory would predict them to be through damping processes.

Another quantity that relates to solar wind fluctuations and waves which shows a speed-dependent relationship is $\delta V \cdot \delta B$ where δ denotes fluctuations relative to the mean. This is best studied by putting the magnetic field in Alfvén units by dividing B by $\sqrt{4\pi\rho}$ where ρ is the mass density of the magnetized fluid. By dividing the total energy we obtain $\sigma_c = (\delta V \cdot \delta B)/E$. This limits the value of $\delta V \cdot \delta B$ so that it becomes a measure of the angle between the velocity vector and the magnetic field vector. It is shown in Figure 2.8 (part of the published analysis covered in Chapter 4) where σ_c is the normalized angle (1 represents anti-parallel propagation relative to the mean field, 0 represents perpendicular and -1 represents parallel). Since the interplanetary magnetic field can be oriented radially inward or radially outward we can multiply σ_c by $-sgn(B_R)$ to obtain a product that is positive for anti-Sunward propagation and negative for Sunward propagation. Figure 2.8 illustrates an interesting

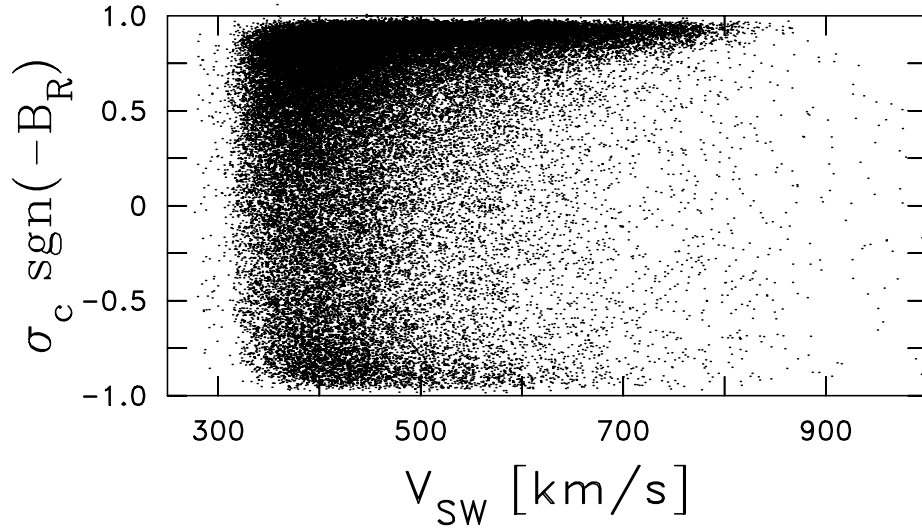


Figure 2.8: This plot shows the degree of correlation between velocity and magnetic field in the solar wind. Most of the time wave propagation is away from the sun, but this analysis show that sunward propagation can occur frequently.

characteristic of $\delta V \cdot \delta B$ which is the maximum for $-\text{sgn}(B_R)\sigma_c = -1.0$. Recall that the core maximum at $-\text{sgn}(B_R)\sigma_c = 1.0$ represents anti-Sunward propagation. The smaller maximum at $-\text{sgn}(B_R)\sigma_c = -1.0$ represents a population of events dominated by Sunward propagating waves.

The plasma waves discussed in this chapter are what make up the large scale structure of turbulence in the heliosphere. As we will see in Chapter 3, an understanding of these waves forms an essential foundation for the study of turbulence and fluctuations.

Chapter 3

Fluctuations

Turbulence describes a fluid whose properties are non-deterministic. The solar wind is an ideal laboratory for in situ turbulence studies because it contains conditions unattainable in a laboratory setting. In the solar wind, the turbulence is driven by fluctuations; these could be fluctuations in the magnetic field, velocity, temperature, density or any other plasma parameter. Understanding these fluctuations can tell us how energy is transferred in the plasma.

3.1 Development of turbulence

It has been shown that the magnetic power in a turbulent plasma “cascades” through a hierarchy of waves. Most of the power resides in the low frequency waves. Damping of the waves causes the energy to cascade from large wavelengths to smaller wavelengths. As it goes through this cascade, energy is removed from the system. This process follows a power law, and the rate of energy dissipation is the spectral index, often referred to as q . In 1941, Kolmogorov published the following formula [18],

$$P_k = C_k \epsilon^{\frac{2}{3}} k^{-\frac{5}{3}} \quad (3.1)$$

where P_k is the power spectrum of the velocity fluctuations, C_k is a universal constant, ϵ is the cascade rate and k is the wave number. Even though this study predates in situ observations, the $-5/3$ prediction has been observed in the solar wind. In turbulence, there exist eddies, which are rotating vortices in the fluid. The time it takes for one rotation is the eddy turnover time. Kolmogorov established the eddy turnover time as $\tau = \frac{\lambda}{v}$ where λ is the size of the vortex and v is the speed. This is a characteristic time scale for turbulence.

In 1965, Kraichnan predicted that the critical timescale of the turbulence is the period of the Alfvén waves rather than the eddy turnover time [19]. This led to a spectral index of $-3/2$ rather than the $-5/3$ prediction of Kolmogorov, described by the following equation:

$$E(k) = A(\epsilon b_0)^{\frac{1}{2}} k^{-\frac{3}{2}} \quad (3.2)$$

where ϵ is the cascade rate (the rate of energy cascade through the inertial range) and k is the wave number.

There are three regimes in the turbulent cascade at 1 AU. Frequencies 10^{-4} Hz (spatial scales greater than 4.5×10^6 km) are considered to be dominated by solar source dynamics (CMEs for example) and are known as the energy containing range that drives interplanetary

turbulence. Frequencies from 10^{-4} Hz to 1 Hz define the inertial range. In this range, power law spectra are observed and the dynamics are thought to be described by energy cascade theories. 1 to 10 Hz (and probably higher) is known as the dissipation range where the power spectral index steepens and dissipation of turbulent energy into heat is thought to occur. Figure 3.2 shows these regimes.

The transition from the inertial range to the dissipation range is likely caused by various dynamics including ion cyclotron damping, and results in the steepening of the spectrum. Thus, the frequency at which this change occurs is near the ion cyclotron frequency.

3.2 Spectral Index

Early studies of plasma fluctuations by Kolmogorov and Kraichnan form an important basis for more modern theories involving the fluctuations. Coleman [8] used magnetic field data from Mariner II to perform a spectral analysis of the plasma waves using actual data. In a subsequent paper [9], the turbulent cascade was shown, with frequency plotted against magnetic power, and the spectral index was shown to be $-5/3$.

Belcher & Davis [3] computed the spectral index for the inertial range several years later. They found that it ranges between -1.5 and -2.2 , and that the fluctuations are not isotropic. This means that the spectral index can change as a function of the angle of the mean magnetic field with respect to the radial direction. Further, they found that the part of the inertial range containing the frequencies 10^{-3} Hz to 10^{-1} Hz has a power law index between -1.6 and -1.7 . However, the lower frequency end of the inertial range (10^{-4} Hz to 10^{-3} Hz) has a larger spread, with indices between -1.5 and -2.2 .

3.3 Geometry

Geometry refers to the orientation of the wave vectors. The wave vectors parallel to the mean magnetic field are known as the slab component and the perpendicular wave vectors are the 2-D component. When studying angular dependence, the angle Θ_{BV} refers to the angle between the wave vector and the mean field. In 1990, *Matthaeus et al.* [24] looked at correlation functions for magnetic fluctuations. For this analysis they used 16 months of ISEE-3 data with 5 minute time resolution and analyzed spatial scales of 7.2×10^4 to 4×10^6 km. The result, known as the “Maltese Cross” (displayed in Figure 3.1), shows that most of the power resides parallel and perpendicular to the mean field, and that intermediate angles have significantly reduced magnetic power.

In 1995, Goldreich and Sridhar [12] postulated that the spectral index has an angular dependence. They stated that perpendicular fluctuations are dominated by the timescale of wave propagation while parallel fluctuations are dominated by the timescale of perpendicular fluctuations. This is known as the critical balance assumption. The critical balance assumption means that the spectral index for quasi-perpendicular fluctuations is -2 , and the spectral index for quasi-parallel fluctuations is $-5/3$. Goldreich and Sridhar showed that for intermediate angles, the spectral index will evolve toward one or the other. As of 2009, this theory is unproven but evidence is gathering for and against it.

Bieber et al. [4] established a method for distinguishing slab turbulence and 2-D turbulence. They used a correlation matrix to compute where the power is. *Bieber et al.* assume a simplified model in which there are only perpendicular and parallel wave vectors. By taking

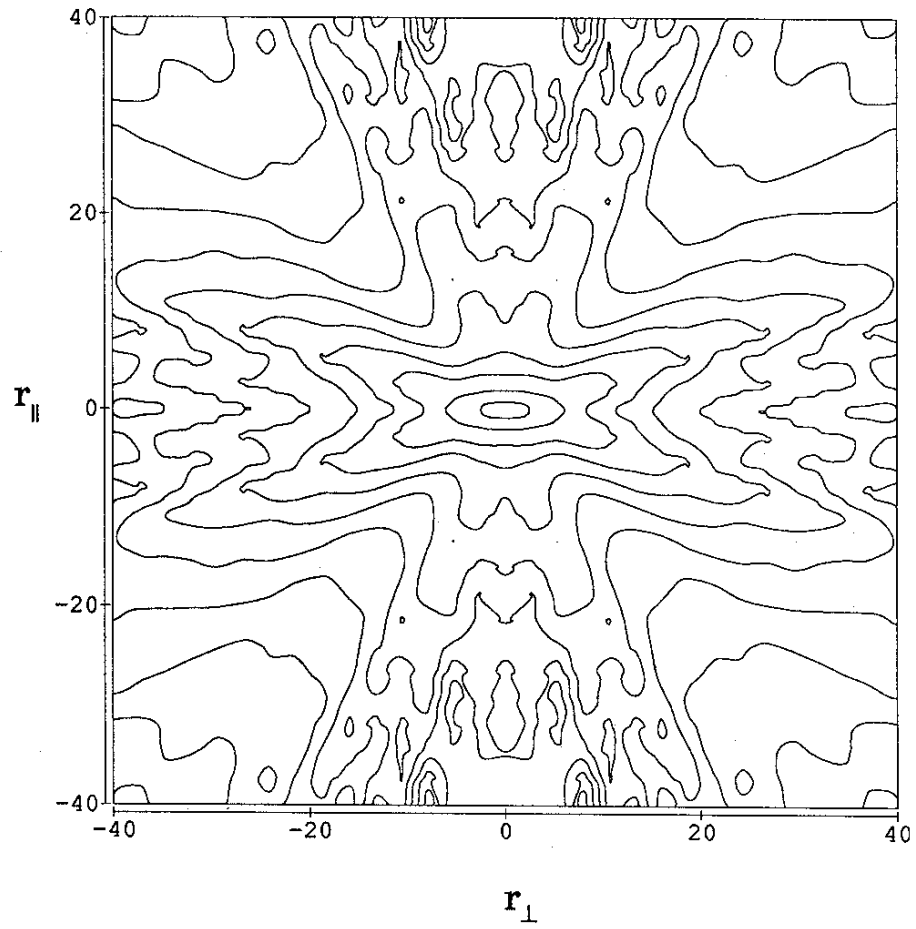


Figure 3.1: The Maltese Cross Result [24].

the ratio of power in the perpendicular wave vectors to the power in the parallel wave vectors, they found which component contains more power. The result of this analysis is that 75% of the power is in the perpendicular component. *Bieber et al.* used a second test called the anisotropy test which uses Θ_{BV} , and finds that 95% of the power is in the perpendicular wave vectors. By averaging the results of these two methods, Bieber concludes that about 85% of the power resides in the perpendicular wave vectors.

3.4 Inertial Range

In a low-latitude study of the inertial range using Mariner 2 data, Coleman found a $-5/3$ slope in the magnetic fluctuations that is consistent with the prediction of Kolmogorov [9]. The spectrum of the inertial range appears to be different for magnetic and velocity fluctuations as well. *Podesta et al.* found, using Wind data, that the velocity fluctuations in the solar wind have a spectral index of $-3/2$ [27]. Another aspect of the inertial range spectrum is the dependence of the spectral index on wave vector orientation. Recall that the Critical Balance assumption, postulated by *Goldreich & Sridhar* separates wave vector components by dominating time scale [12]. *Horbury* found a similar result using a wavelet method and high-latitude Ulysses data [15]. The frequency range of *Horbury et al.* is 15 mHz to 98 mHz. *Tessein et al.* conducted a similar study using low-latitude data from the Advanced Composition Explorer (ACE) in the frequency range 1.6 mHz to 16 mHz with structure functions and found no Θ_{BV} dependence [33]. Note that these two studies are looking at different scales, with *Horbury et al.* at the high frequency end of the inertial range and *Tessein et al.* closer to the middle. This issue, as well as the second order structure function method, is discussed further in Chapter 4.

3.5 Dissipation Range

The dissipation range is the steepening of the spectral cascade at small length scales. Prior to the onset of the dissipation range fluid dynamics describe the system. The Navier-Stokes equation represents these fluid dynamics:

$$\frac{\partial v(x, t)}{\partial t} + (v \cdot \nabla)v = \frac{-1}{\rho} \nabla \rho + \nu \nabla^2 v \quad (3.3)$$

The MHD equations break down at the onset of dissipation because they are only valid at lengths greater than the ion inertial scale. This scale, λ_{ii} , is given by the following equation:

$$\lambda_{ii} = \frac{\nu_A}{\Omega_{ic}} \quad (3.4)$$

where ν_A is the Alfvén speed and Ω_{ic} is the ion cyclotron frequency [11]. The ion inertial scale represents the breakdown of single fluid theory, and the increasing importance of ion kinetics where the dissipated waves are converted into heat.

The major characteristic of the dissipation range is the steepness of its spectrum, which was explored by *Leamon et al.* [20, 21]. *Leamon et al.* analyzed both the inertial and dissipation ranges using ACE data. They found a well-formed Kolmogorov spectrum in the inertial range ($q = -1.66$). The value of q found for the dissipation range was -3.04 , but ranged between -2 and -5 . Leamon also found the power in the dissipation range to be 46%

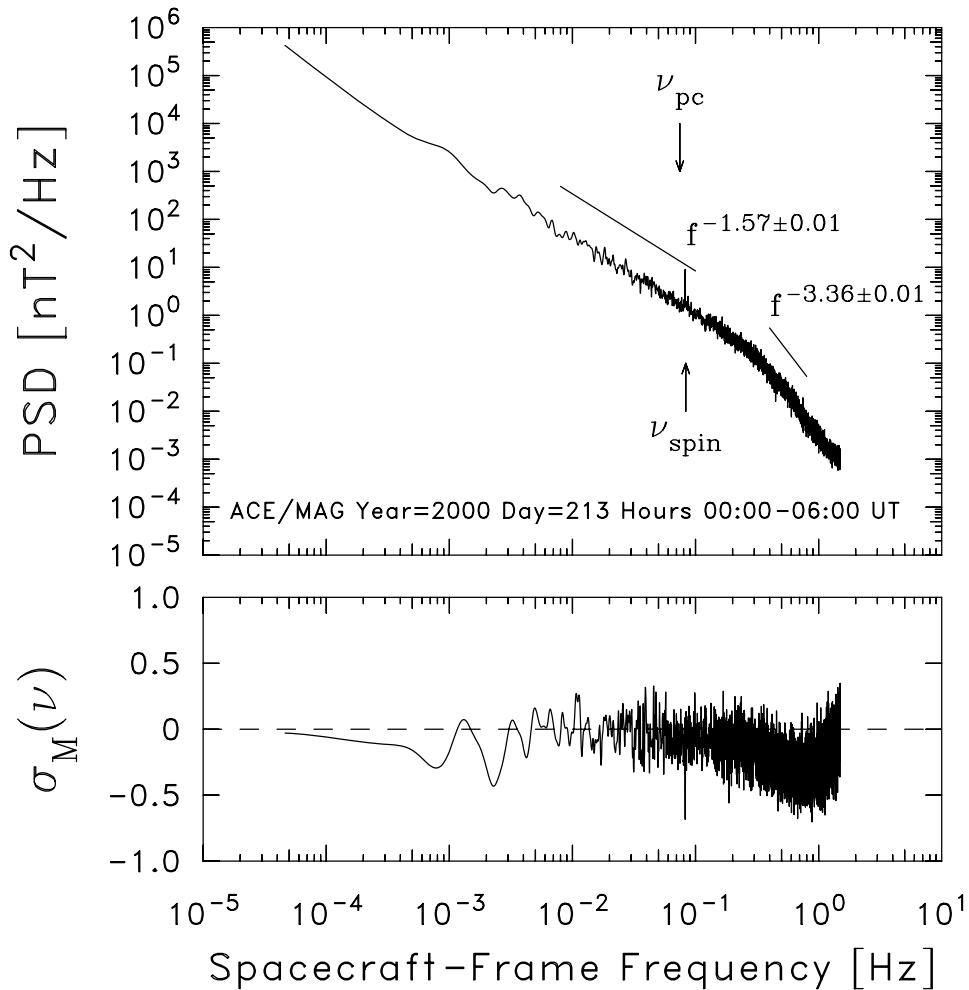


Figure 3.2: The power spectrum. Notice the frequency at which the slope changes. This marks the transition from the inertial range to the dissipation range [14].

slab and 54% 2-D. This is a greatly increased slab fraction from the inertial range, which typically has values of around 11% for the slab component. *Smith et al.* investigates why the dissipation range spectral index varies more than that of the inertial range [31]. They found that the steepness of the dissipation range is dependent on the cascade rate in the inertial range.

3.6 Helios Observations

The Helios spacecraft in the late 1970s permitted solar wind measurements close to the Sun for the first time. Helios took measurements between 0.3 AU and 1 AU. *Bavassano et al.* [2] computed spectral indices from Helios observations and found only a slight radial evolution. Values found from this analysis range from 1.5 to 1.65 at 0.29 AU and 0.87 AU respectively. This indicates that the spectral index can change with heliocentric distance, however, the change is minimal.

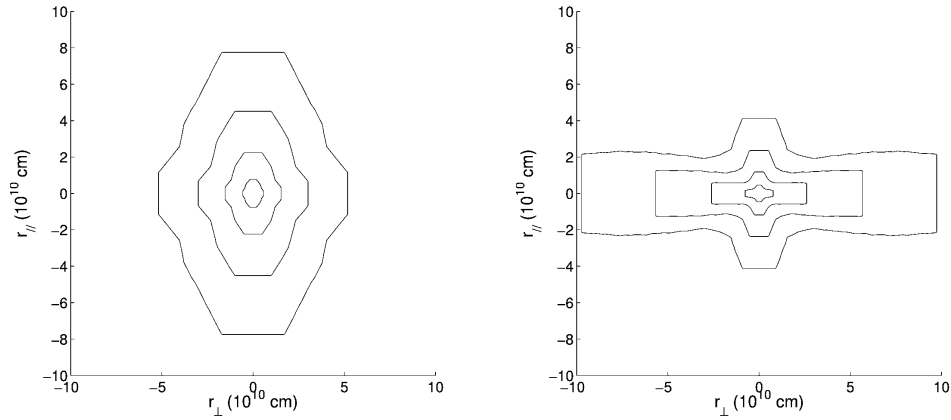


Figure 3.3: Result of separation between fast and slow wind. Slow wind (left) has more power in the perpendicular direction because of the larger gradient in that direction. Fast wind (right) has a larger gradient in the parallel direction [10].

3.7 Differences Between Fast and Slow Wind

In addition to the plots displayed in Chapter 2 where the differences between fast and slow streams are shown, there exist differences in the fluctuations as well. *Dasso et al.* [10] extend the two dimensional analysis of *Matthaeus et al.* [24], and separate the solar wind into fast and slow subsets on a spatial scale of 5×10^4 to 10^6 km. Any stream slower than 400 km/s was defined as slow wind, and faster than 500 km/s was defined as fast wind. Anything between 400 and 500 km/s was excluded to better separate the two populations. This analysis used five years of data from Advanced Composition Explorer (ACE). Using correlation functions for large scale fluctuations in the inertial range, they found that fast solar wind is dominated by quasi-parallel fluctuations and slow solar wind is dominated by quasi-perpendicular fluctuations. This result is shown in Figure 3.3.

3.8 Smaller Scale Analyses

Two publications in 2006 by *Smith et al.* and one in 2008 by *Hamilton et al.* [14, 31, 32] study turbulence at smaller scales from the analyses discussed above. This high frequency regime is unresolved by most plasma instruments, including the one aboard the ACE spacecraft.

The first paper, *Smith et al.* [32], focuses on the ratio of magnetic power in the component perpendicular to the field to the magnetic power in the parallel component (this is known as the variance anisotropy). The variance anisotropy, defined as $\frac{\delta B_{\perp}^2}{\delta B_{\parallel}^2}$, may be a proxy for density fluctuations in the high frequency range because the density seems to scale with magnetic power in the parallel fluctuations. Earlier studies predict that the variance anisotropy should be correlated to proton beta, β_P [32]. *Smith et al.* found that variance anisotropy varies as $\beta_P^{-0.7}$ (Figure 3.5). Earlier studies also predict a correlation between variance anisotropy and fluctuation level $\frac{\delta B}{B_0}$. *Smith et al.* also find this correlation in both open and closed magnetic field lines (Figure 3.4). Does this mean that β_P and fluctuation level are correlated? Figure 3.4 shows that these seemingly unrelated quantities are proportional and includes further relationships.

Hamilton studied the variance anisotropy further in a 2008 publication [14] (this is de-

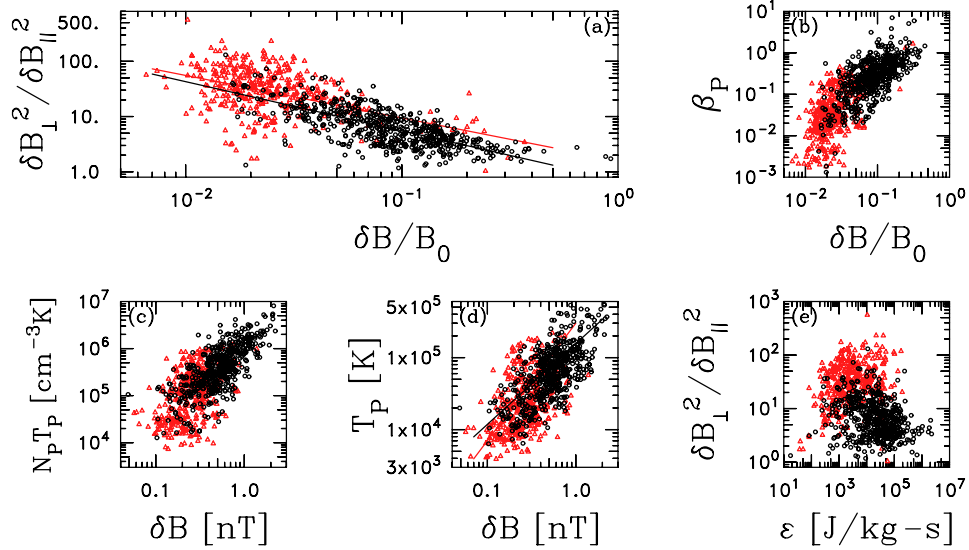


Figure 3.4: In all plots red represents magnetic clouds and black represents open field lines. (a) Variance anisotropy vs. $\delta B/B_0$. (b) β_P vs. $\delta B/B_0$. This shows correlation between seemingly unrelated quantities. (c) $N_P T_P$ vs. δB showing correlation between quantities not causally connected. (d) T_P vs. δB . (e) Plot of variance anisotropy vs. cascade rate ϵ . This shows that variance anisotropy is not well correlated to the rate of energy cascade [32].

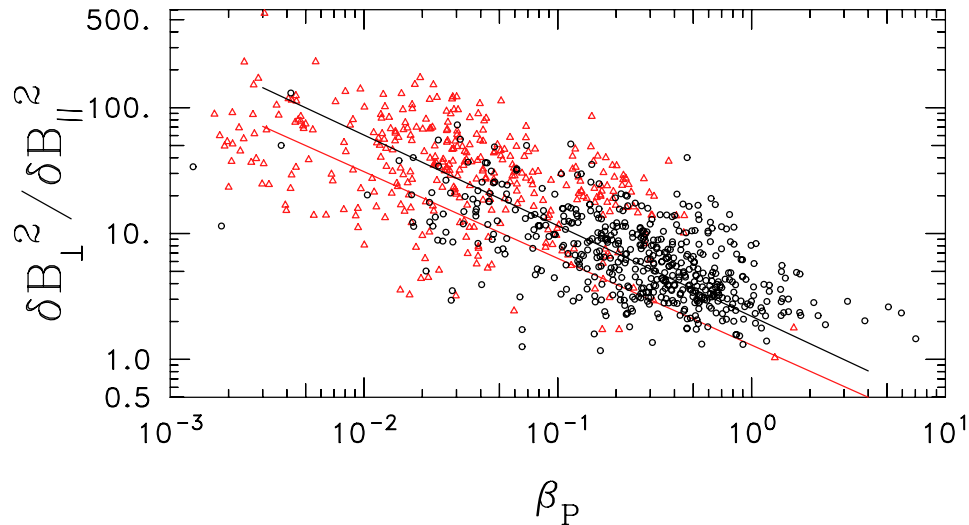


Figure 3.5: Computed magnetic variance anisotropy vs. β_P . Red represents magnetic clouds and black represents open field lines [32].

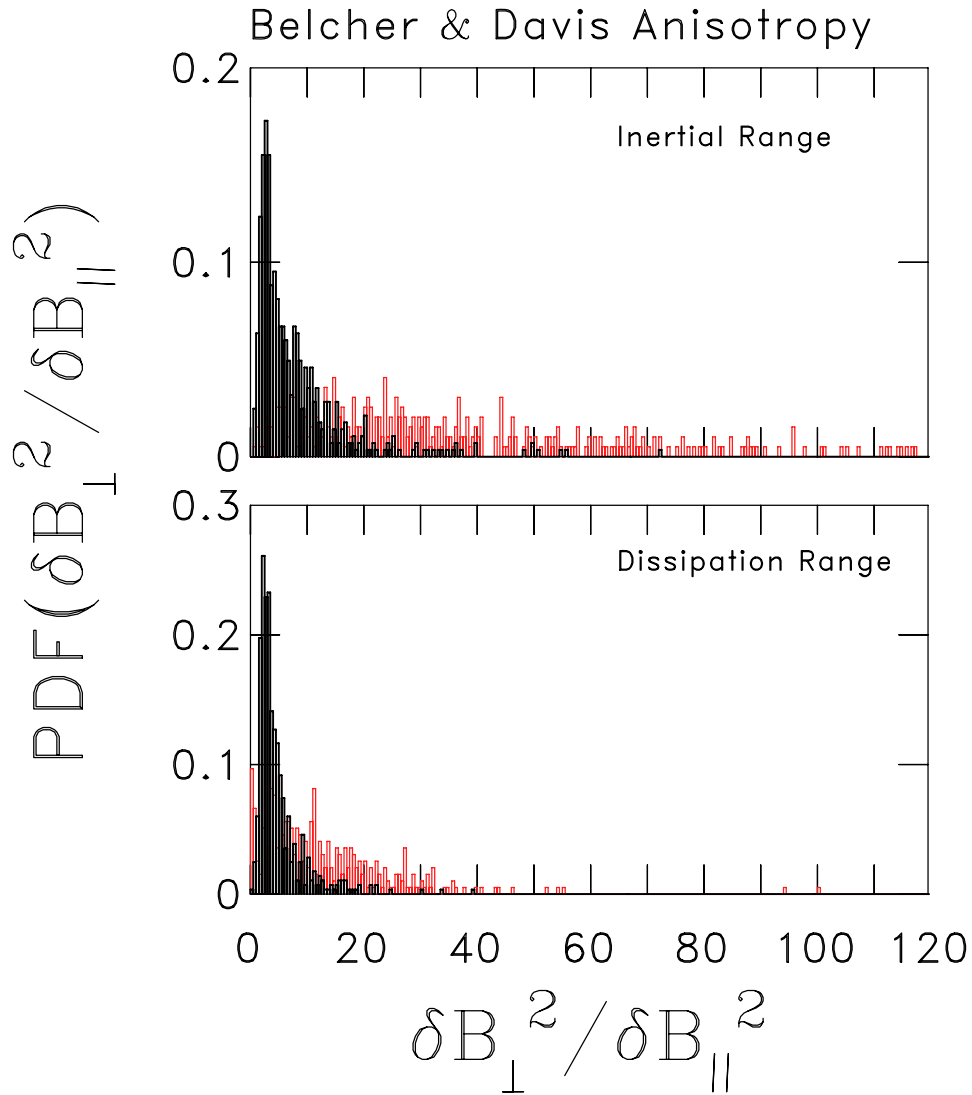


Figure 3.6: Distribution of magnetic variance anisotropy. Black represents open field lines and red represents magnetic clouds [14].

scribed in more detail in Section 4.2.2). Figure 3.6 shows the distribution functions for magnetic variance anisotropy. Note that magnetic clouds have high anisotropy in the inertial range but not in the dissipation range. Figures 3.7 and 3.8 show a scatter of variance anisotropy in the inertial range vs. dissipation range. The inertial range anisotropy is greater than dissipation range anisotropy which tells us that the dissipation range is generally more compressive (recall that this is because the density scales proportionally to the parallel magnetic fluctuations).

Leamon et al. [21] showed for the first time that there exists a strong correlation between the magnetic helicity in the dissipation range (normally associated with cyclotron damping) and the cross helicity in the inertial range (normally associated with propagation direction). Magnetic helicity is defined by the following equation:

$$\sigma_M = \left\langle k \frac{A(k) \cdot B(k)}{\sqrt{E_B(k)}} \right\rangle \quad (3.5)$$

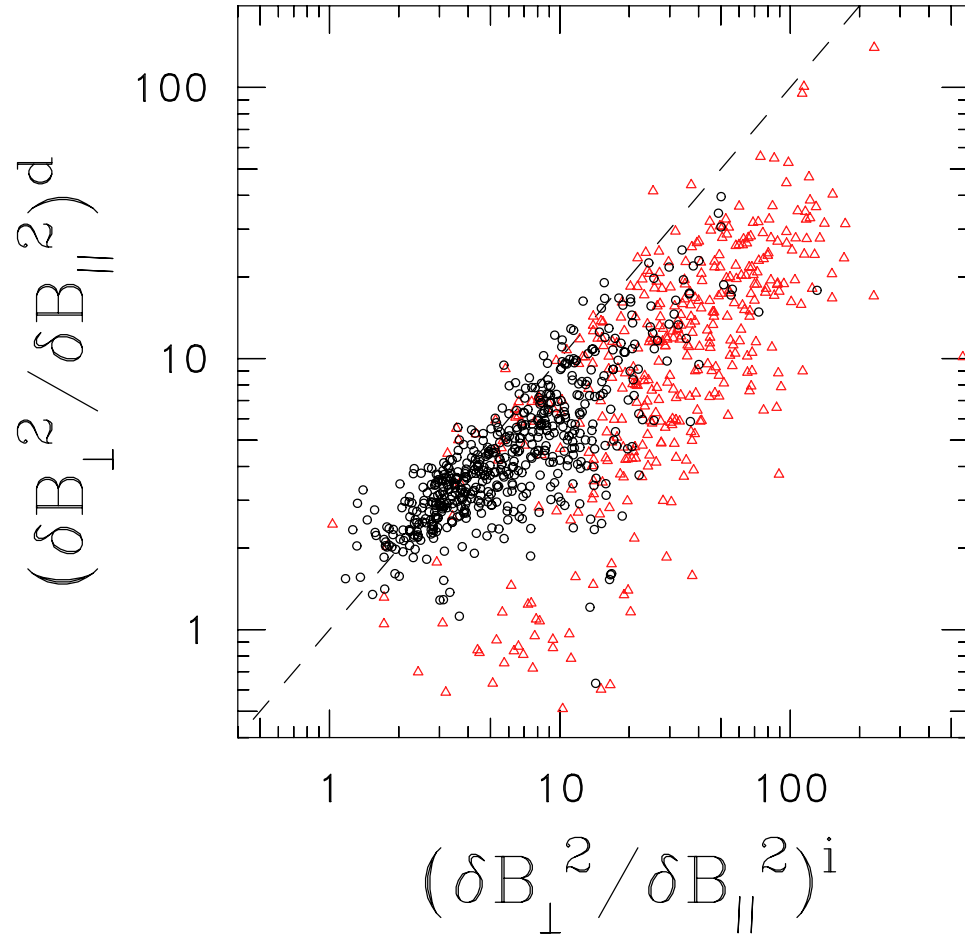


Figure 3.7: Scatter of variance anisotropy plotting inertial range against dissipation range. Black represents open field lines and red represents magnetic clouds. Note that the dissipation range is more compressive [14].

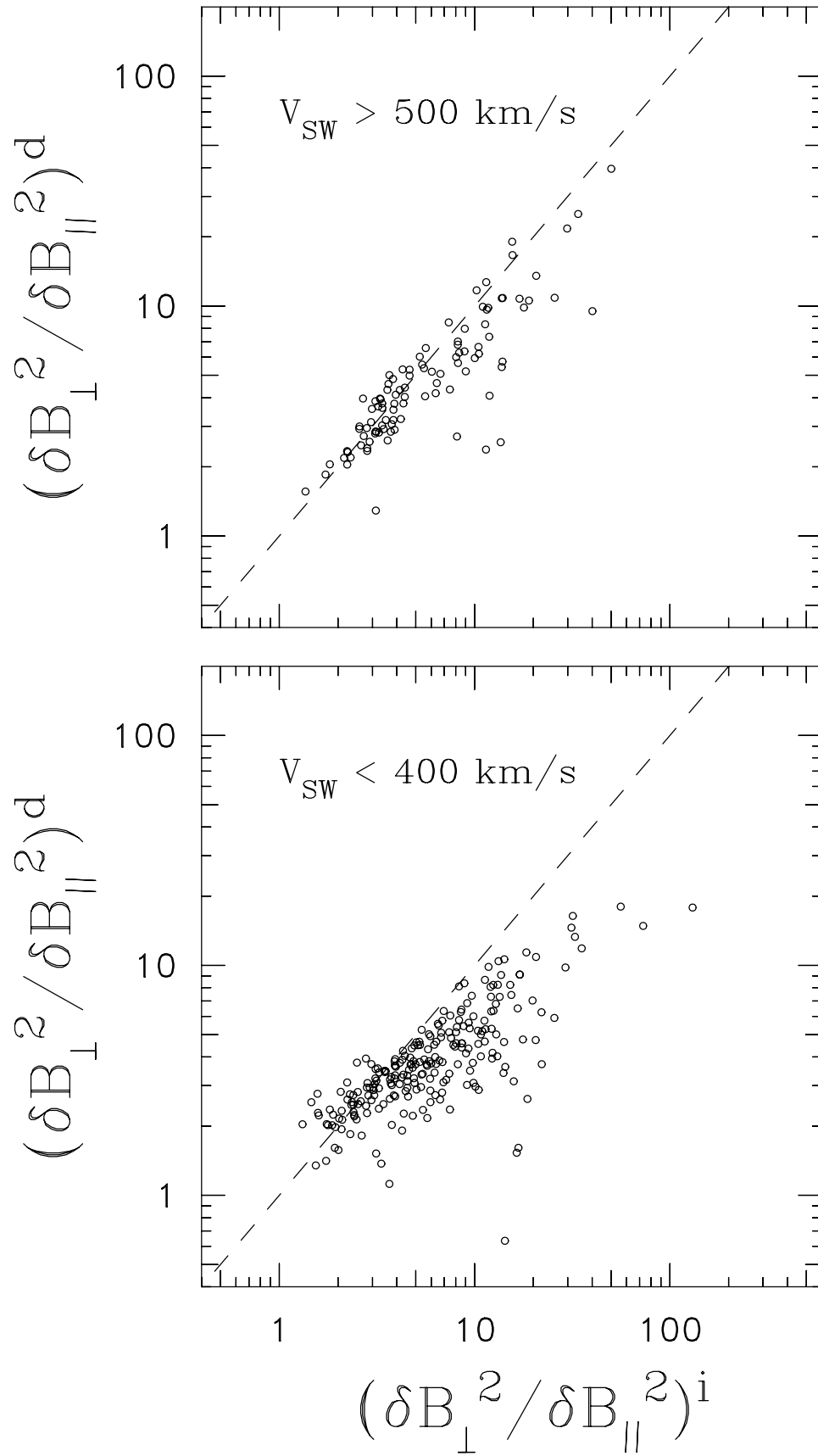


Figure 3.8: Same as Figure 3.7 but subsetted for wind speed [14].

where $E_B(k)$ is the magnetic energy spectrum. Cross helicity is,

$$\sigma_c = \left\langle \frac{2\delta V \cdot \delta B}{\delta V^2 + \delta B^2} \right\rangle \quad (3.6)$$

where γ_r represents cyclotron damping, which means that Alfvén waves are picked out, while γ_0 represents everything besides Alfvén waves. Their theory argues that $\frac{\sigma_r}{\sigma_M} = -(1 + 2\gamma_0/\gamma_r)$. They obtain $\frac{\sigma_r}{\sigma_M} = -2.4$, which leads to $\frac{\sigma_c}{\sigma_M} = 0.7$. Figure 3.9 shows Hamilton’s cross helicity analysis. Hamilton finds that $\sigma_c \sim -2.4\sigma_M$.

In traditional hydrodynamics, the scale at which the dissipation range appears is dependent on the cascade rate of the inertial range. *Leamon et al.* showed that the appearance of the dissipation range in the solar wind does not follow predictions derived from fluid viscosity and resistivity [20]. However, they did find that the dissipation range dynamics are in agreement with kinetic plasma theory. *Smith et al.* found that the spectral form of the IMF dissipation also does not adhere to the hydrodynamic predictions of Kolmogorov [18] and that the appearance of the dissipation range has no dependence on the cascade rate [31] (Figure 3.11). However, they found that the steepness of the dissipation range spectrum is dependent on the cascade rate (Figure 3.10). Given that the fluid approximation in the solar wind breaks down at scales where the dissipation range begins, *Smith et al.* conclude that the onset of the dissipation range represents a coupling of a fluid cascade approximation and kinetic dissipation. They also conclude that the traits of the inertial range have nothing to do with the onset of dissipation and that traditional hydrodynamics is not a good approximation for the dissipation range.

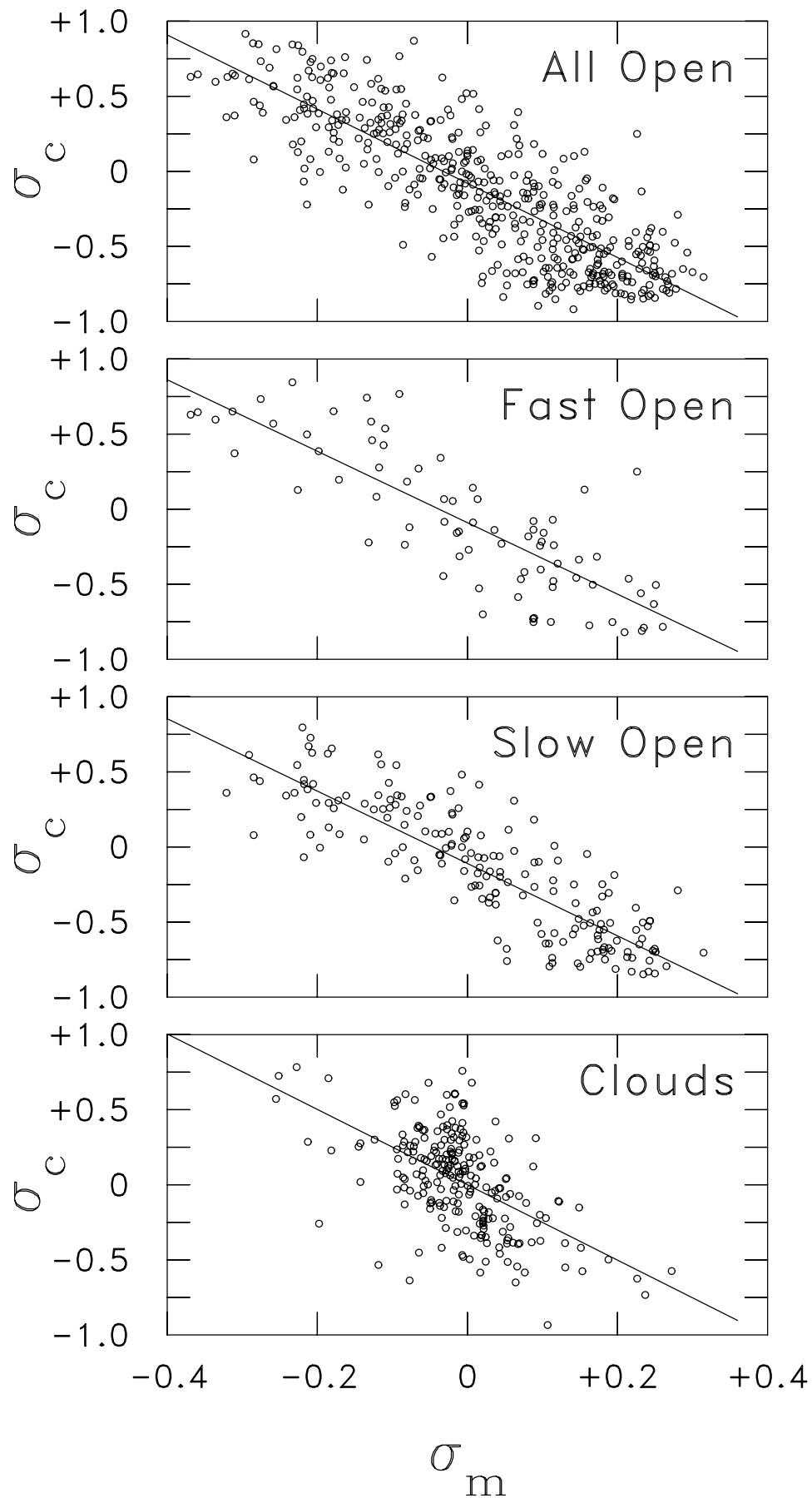


Figure 3.9: Comparison of $\langle \sigma_c \rangle$ to $\langle \sigma_M \rangle$ in the inertial range [14].

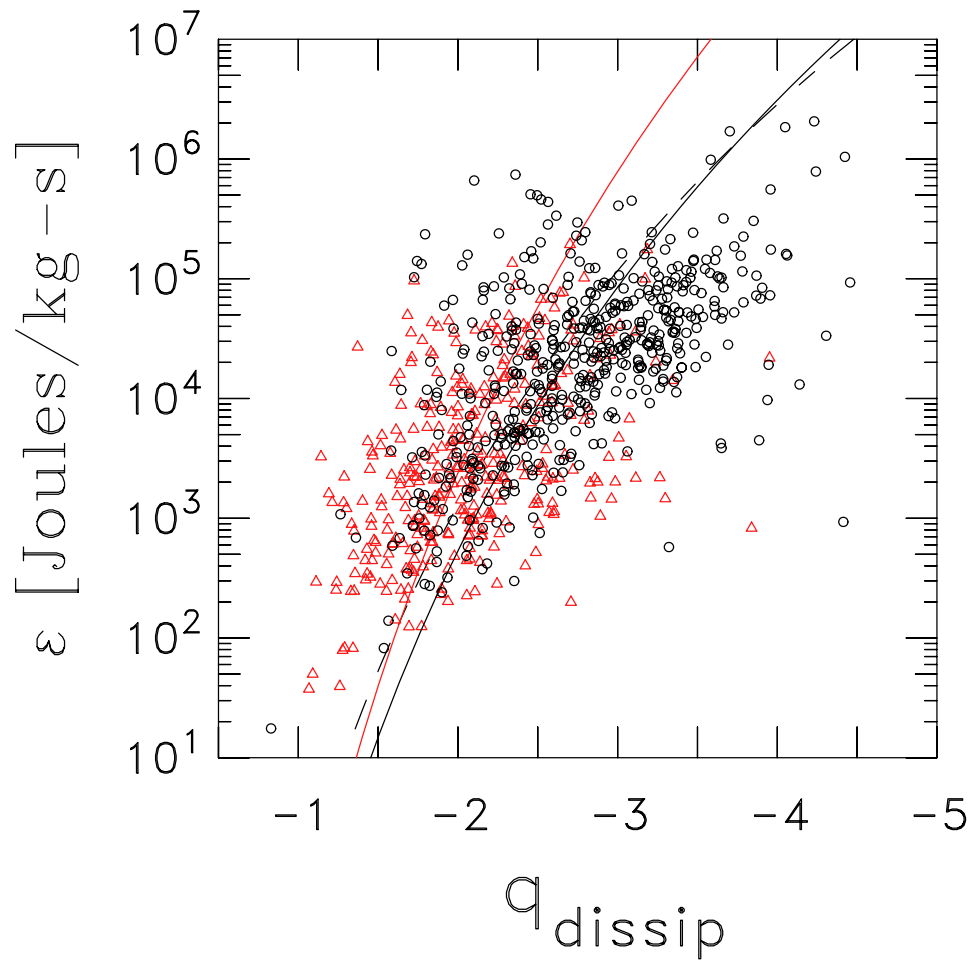


Figure 3.10: Plot of cascade rate ϵ vs. dissipation range spectral index q_{dissip} . The spectral form of the dissipation range is dependent on the cascade rate.

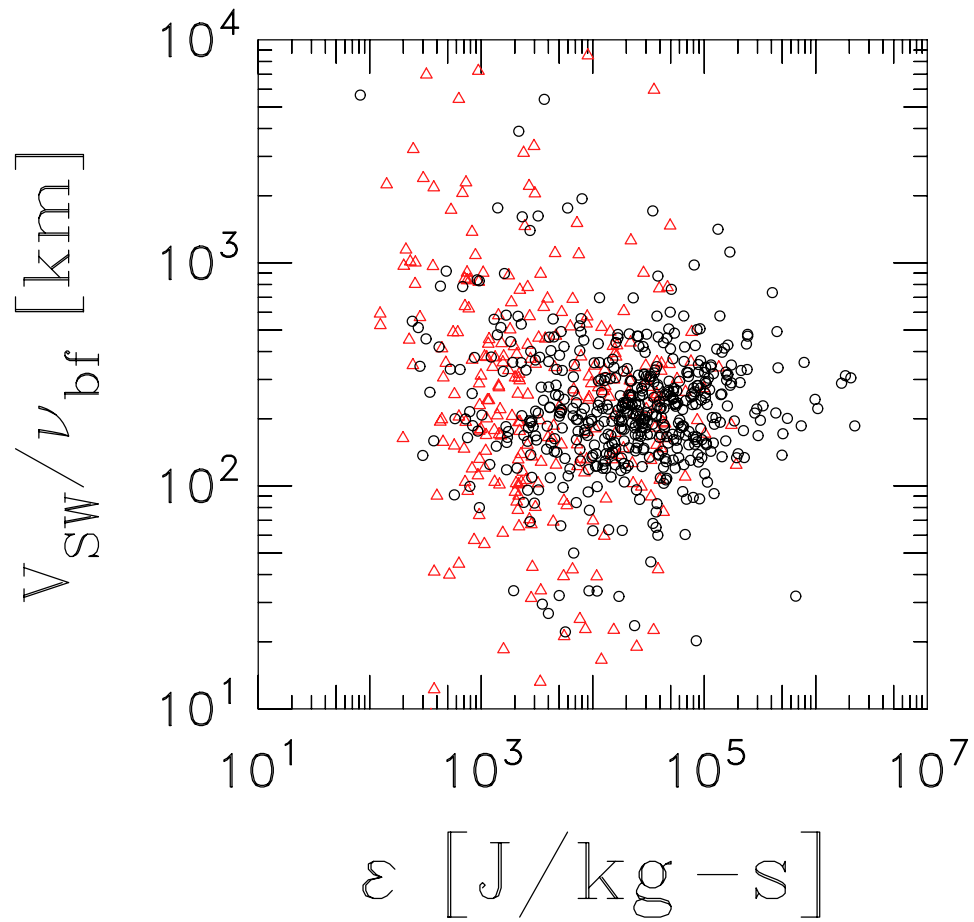


Figure 3.11: The length scale of the spectral break V_{SW}/ν_{bf} vs. cascade rate ϵ . Traditional hydrodynamics predicts that the cascade rate correlates to the onset of dissipation. However, there is no correlation here [31].

Chapter 4

Tessein Hourly Analysis

The Tessein Hourly Analysis is presented here as a precursor to the CIR study. It was taken up by the author in 2006 and published February 2009 [33]. The purpose of the study was to look at distinctions in the dynamics between parallel and perpendicular spectra in the inertial range. In addition, we looked to resolve evidence of different spectral forms for the perpendicular fluctuations and search for an anisotropic spectrum by focusing on power law indices. We did this by looking at how the power law index changes with Θ_{BR} (as explained in Chapter 3) and extending previous results to the current study.

4.1 Background

MHD turbulence in the presence of a magnetic field has two distinct timescales, the eddy turnover time, $\tau_{nl}(k) = \frac{1}{ku_k}$ and the Alfvén propagation period, $\tau_A(k) = \frac{1}{k_{\parallel}V_A}$, where V_A is the Alfvén speed $V_A = \frac{B_0}{\sqrt{4\pi\rho}}$, and k is the wave number. In traditional hydrodynamics, there is only the eddy turnover time and this is what Kolomogorov used to obtain the $-5/3$ prediction [18]. The *Goldreich & Sridhar* model attempts to separate these two timescales [12] and is shown pictorially in Figure 4.1. This theory creates a separatrix which establishes in what angles the dominant timescales apply. It shows that nonlinear timescales dominate quasi-perpendicular fluctuations while wave-like time variations dominate the quasi-parallel fluctuations. This results in a spectral index of -2 at small angles of Θ_{BV} and $-5/3$ at angles near perpendicular. Intermediate angles will evolve between -2 and $-5/3$. This is known as the critical balance assumption.

Horbury et al. studied this further using a wavelet analysis [15]. This study used high-latitude Ulysses data at 1.4 AU on a high speed stream coming out of a polar coronal hole. The wavelet analysis was used to compute the power spectra in the frequency range 15-98 mHz. This range is the high frequency end of the inertial range. The result they found is consistent with the critical balance assumption. All this leads up to the publication of *Tessein et al.* [33]. *Tessein et al.* look at this further using the second order structure function method [30].

4.2 Data Analysis

The data for this study comes from three distinct data sets. The first is a database consisting of almost all of the ACE data from 1998 through 2007. It has 64 s resolution, and is analyzed

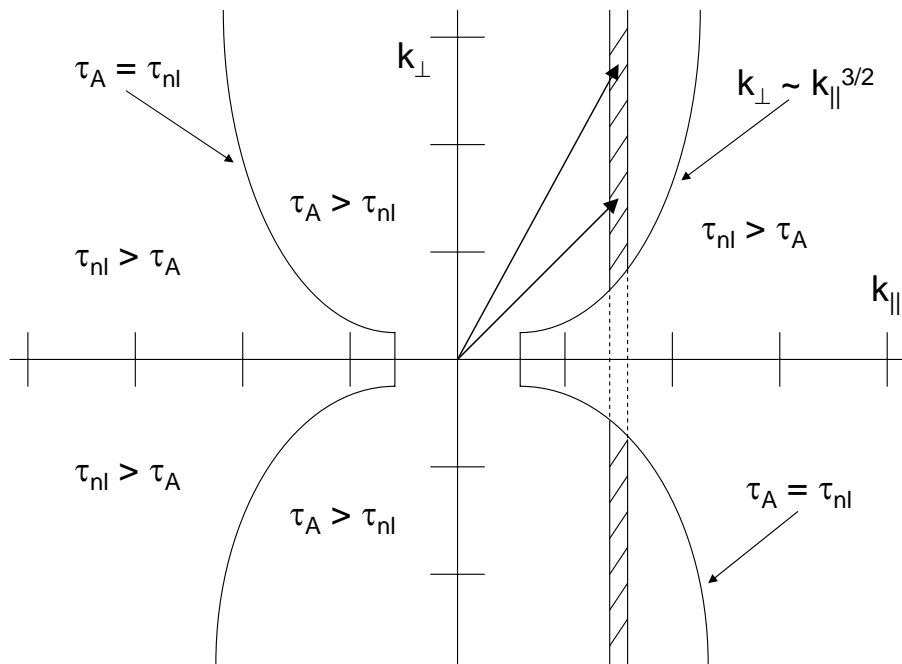


Figure 4.1: The Goldreich & Sridhar model. Axes are the perpendicular and parallel fluctuations, and the curved lines denote the boundary between regions dominated by a particular timescale.

in the frequency range of 1.6 to 16 mHz (the middle of the inertial range). There are roughly 74,000 data points. The second dataset used is that of Hamilton [14]. This dataset comes from ACE as well and consists of 960 hand picked intervals with 393 intervals from 28 magnetic clouds from the years 1998 through 2002 (solar maximum years). This data has a 3 vector/s magnetometer resolution and analyzes the frequency range 10 to 200 mHz (high freq. end of the inertial range). The third dataset comes from the Helios 1 spacecraft during a solar minimum period. This consists of 380 hand picked intervals between 0.3 and 1 AU. This data has a 6 vector/s resolution and the frequency range analyzed is 5 to 20 mHz. Note that the Hamilton data set covers the same scales as Horbury.

4.2.1 ACE 64 s Merged Data

The ACE data consists of merged data from the ACE SWEPAM and MAG instruments. This data covers the time interval from day 23 of 1998 to day 56 of 2007. The vectors in the data are in the RTN coordinate system where R stands for Radial, T stands for transverse, N stands for Normal and $R \times T = N$. The solar wind nominally flows in the $+R$ direction unless it is deflected by upstream ejecta. The RT -plane is the Sun's equatorial plane, and the $+N$ direction is solar north. The data is subsetted to one hour intervals, and associated uncertainties are calculated. The data then goes through a linear detrend, and variances with uncertainties are computed.

At this point, second order structure functions are obtained from 1-10 points, which represents a lag of 64 to 640 s. The structure function is defined by the following equivalence (for parameter $Z(x)$)[30]:

$$S_2(L) = \langle [Z(x) - Z(x + L)]^2 \rangle \quad (4.1)$$

where $\langle \dots \rangle$ denotes ensemble average, and L is the lag. This is done for each component, and the diagonal elements of the resulting matrix are summed to obtain the magnetic trace. Resulting structure functions are fit to the form $S_2(L) = AL^n$, where $q = -(n + 1)$ is the implied index of the power spectrum. Then the same is done for the velocity, and the results of the structure functions are fit to a power law form.

Figure 4.2 shows distributions of computed structure function indices. Recall that these are related to the spectral index by the equivalence $q = -(n + 1)$. These plots display the distribution of fitted power law indices and how often each occurs. B_n is plotted for having very few current sheet crossings which can contaminate the samples. We include V_n because changes in the R component of solar wind velocity over the course of an hour can dominate the trace. The N component is not subject to as much large scale change, and is useful for this analysis. We further subset the data into fast and slow wind as defined by *Dasso et al.* [10]. Wind speed in the subsets are based on wind speed averaged to a one hour interval.

We see from the plots that the most probable value for n is $2/3$ which corresponds to $q = -5/3$. V_n is centered near $1/2$, which corresponds to a $-3/2$ spectral index. This magnetic field/solar wind duality is consistent with the findings of Podesta [27], where the $-5/3$ magnetic field spectral index agrees with the Kolmogorov [18] spectrum and the $-3/2$ velocity spectral index agrees with the prediction of Kraichnan [19]. Also, note that the N components of \mathbf{B} and \mathbf{V} are about the same as the trace, which eliminates the need to worry about current sheet crossing and large scale velocity changes. Also recall the predicted spectral index of -2 from *Goldreich & Sridhar* [12], and observed by *Horbury* [15]. We see -2 , but it is very uncommon. The discrepancy between *Tessein et al.* and *Horbury et al.* may have to do with timescales.

Figure 4.3 shows computed uncertainties for the fits. Uncertainties are less than 0.1 and well determined, so good statistics have been obtained. We have computed error-weighted means of the form:

$$\langle n \rangle \equiv \sum_i (n_i / \sigma_i^2) / \sum_i (1 / \sigma_i^2) \quad (4.2)$$

where n_i is an individual fit index and σ_i is the error associated with the fit. We can then compute the variance of the associated distribution:

$$\langle \sigma_{stddev}^2 \rangle \equiv \sum_i (n_i - \langle n \rangle)^2 / \sum_i (1 / \sigma_i^2) \quad (4.3)$$

The two sources of error are individual measurement error and the width of the distribution. We define the error-of-the-mean as:

$$\sigma_{err}^2 \equiv (1/N)\sigma_{stddev}^2 + 1 / \sum_i (1 / \sigma_i^2) \quad (4.4)$$

Error-of-the-mean is smaller than the plot symbol because each bin contains hundreds of points and in some cases, thousands. Note that a spectral index of -2 is more than one standard deviation off the mean, meaning that its occurrence is rare.

Figure 4.4 shows computed indices in the same manner as the above analysis. In this case the computed power-law indices are a function of Θ_{BR} and separated into 5° bins where error bars represent standard deviation. The plots show that there is no statistically significant Θ_{BR} dependence. The spectral index shown in this plot is consistent with the most probable values from Figure 4.2 and the standard deviations are comparable to the width of the distributions in Figure 4.2. This means that -2 is consistently more than one standard deviation from the mean for all values of Θ_{BR} .

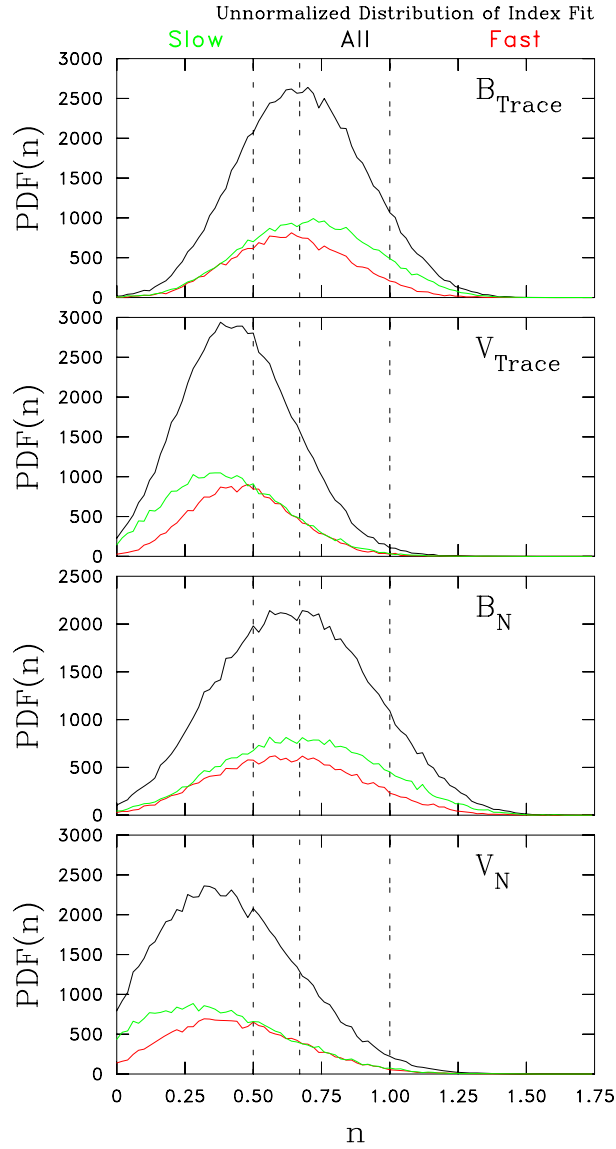


Figure 4.2: Analysis using ACE data from 1998 through 2007 with 64 s data resolution averaged to one hour intervals. The top panel shows the distribution of fitted power law indices for the \mathbf{B} tensor. The second panel shows the distribution of fitted power law indices for the \mathbf{V} tensor. The third panel shows the distribution of fitted power law indices for the north-south component of the \mathbf{B} tensor. The fourth panel shows the distribution of fitted power law indices for the north-south component of the \mathbf{V} tensor. Dashed lines indicate $n = 0.5, 0.67$ and 1.0 ($q = -1.5, -5/3$ and -2 respectively).

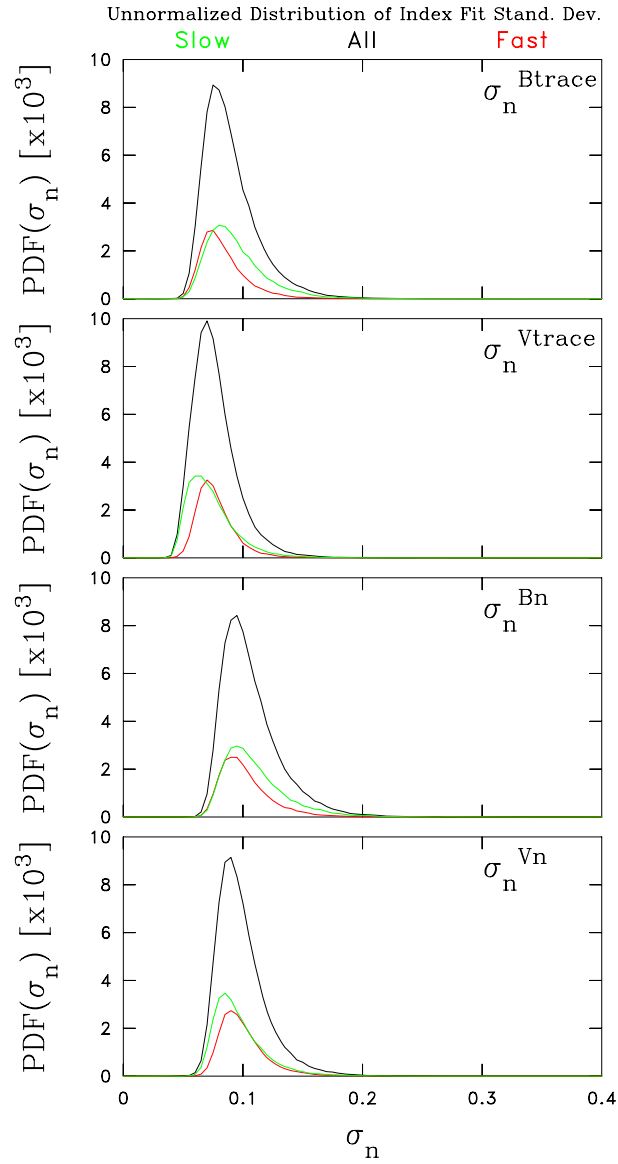


Figure 4.3: The distribution of computed uncertainties in power law indices for each fitted interval.

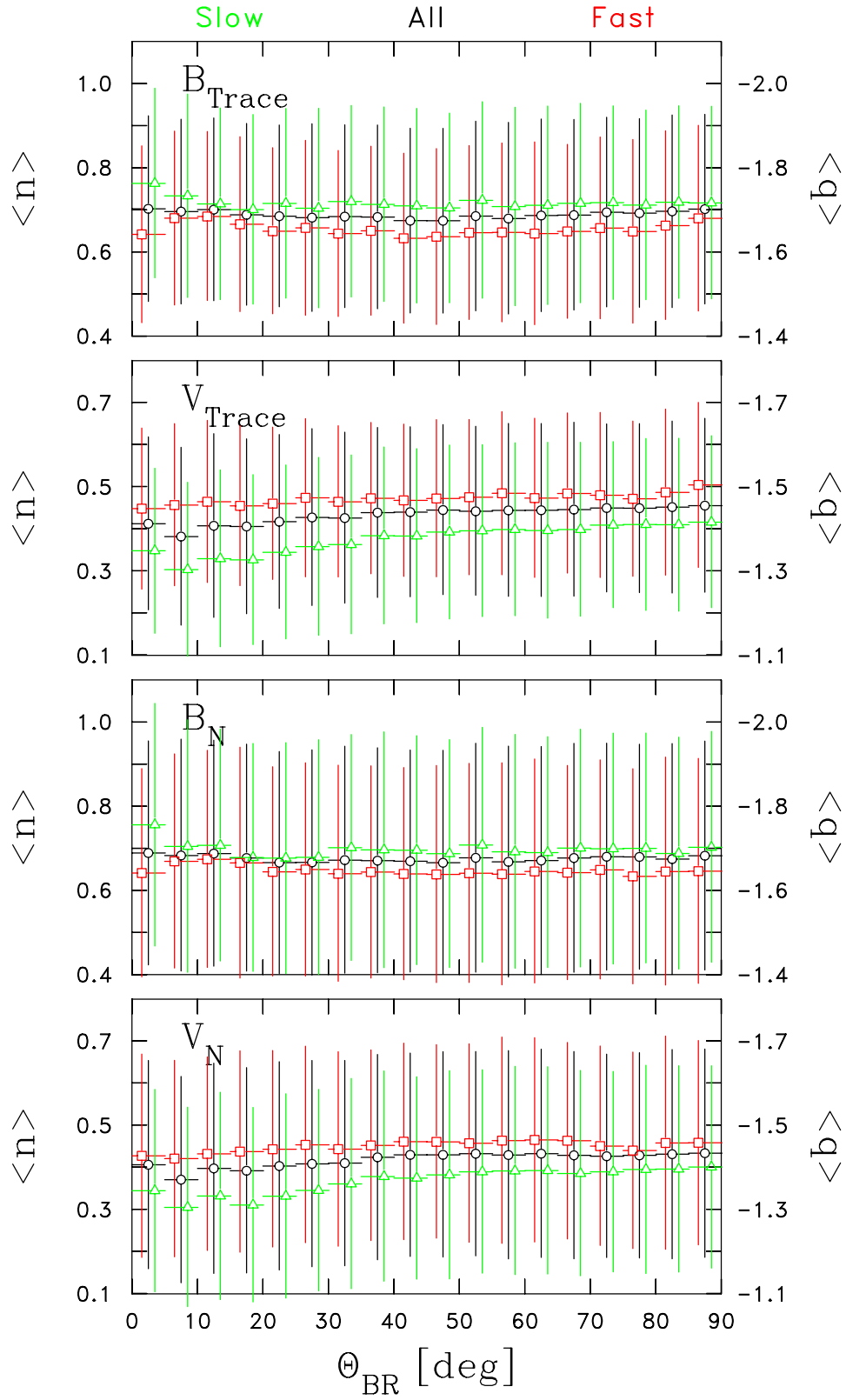


Figure 4.4: Same analysis as Figure 4.2 but fitted power-law indices are a function of Θ_{BR} .

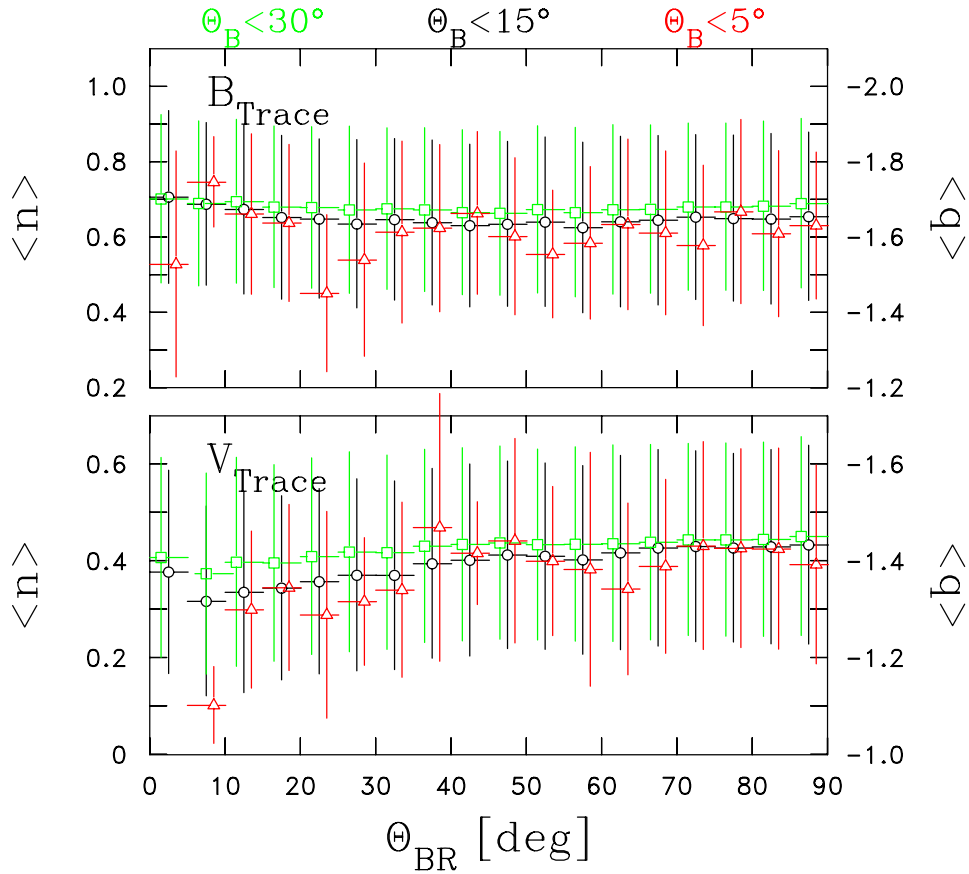


Figure 4.5: Same analysis as Figure 4.4 but samples are limited to those hours when Θ_B is smaller than the prescribed angle.

The amount of points in each bin varies. The B_{trace} distribution for $40^\circ < \Theta_{BR} < 45^\circ$ contains 5793 estimates of n_i . The computed $\langle n_i \rangle$ is 0.674 while the computed standard deviation is 0.219 and the error-of-the-mean is 0.003. For the bin $0^\circ < \Theta_{BR} < 5^\circ$ there are 384 estimates of n_i . The computed $\langle n_i \rangle = 0.702$ while the computed standard deviation is 0.22 and the error-of-the-mean is 0.01. If the Goldreich & Sridhar prediction is to be viewed as a partial theory that only holds under certain conditions, then it is 1.4 standard deviations away from the mean. However, if it is a universal theory for MHD then its predictions are 30 standard deviations away from the mean.

It has been said that the wavelet analysis used by *Horbury et al.* better resolves small- Θ_{BR} . We can address the discrepancy with *Horbury et al.* by limiting our analysis to small fluctuations of instantaneous Θ_{BR} . This is also helpful because the *Goldreich & Sridhar* prediction is based on the assumption that the mean field is much larger than the fluctuations in the magnetic field. To do this, we define $\Theta_B \equiv \arctan(B_{\perp,rms}/|B_0|)$ where $B_{\perp,rms}$ is the root-mean-square variation of the component of the magnetic field perpendicular to the mean field direction. In this way Θ_B becomes a measure of the variability of the field direction and intervals with both small Θ_{BR} and small Θ_B can be inferred to sample the τ_A dominated region of the spectrum without contamination from the τ_{nl} dominated portion of the spectrum. Figure 4.5 shows the computed indices for values of Θ_B less than 5° , 15° , and 30° . These small angle bins tend to be very depopulated; there are only nine intervals for $\Theta_{BR} < 10^\circ$ and $\Theta_B < 5^\circ$. Even though these bins do not produce good statistics there is no

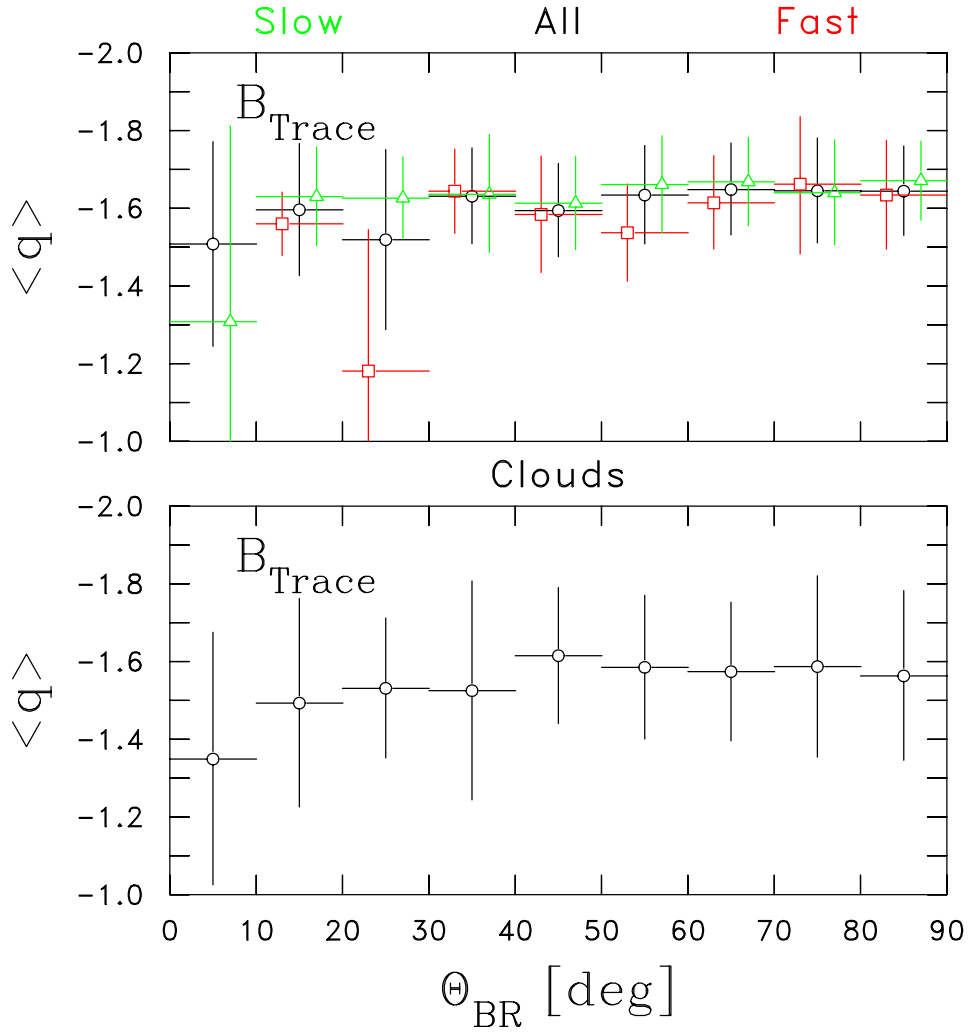


Figure 4.6: Means and variances for fitted power law indices as a function of Θ_{BR} using the Hamilton database. Top: Mean indices for all open field lines (black), fast wind open field lines (red), and slow wind open field lines (green). Bottom: Mean indices for all magnetic clouds.

trend toward $q = -2$. The spectral index is still $-5/3$ for the magnetic field and -1.4 for velocity.

4.2.2 ACE High Resolution MAG Data Analysis

This analysis comes from a data set known as the Hamilton database [14]. Recall that the Hamilton database consists of 960 intervals from solar minimum years. The intervals, one to three hours in duration, are handpicked to contain a broad range of solar maximum conditions, including 28 distinct magnetic clouds. In order to keep the data as pure as possible, there are no shocks present in this database. The spectra were fit to two distinct frequency ranges and only those with proper power law form were retained. The purpose of this database was to test the conclusions of various earlier papers. The analysis found a spectral index of $-5/3$ for the inertial range and $-5/2$ for the dissipation range.

We apply the above dataset to the analysis from Section 4.2.1. The data used here has a resolution of 3 vectors / s and is analyzing the high frequency end of the inertial range,

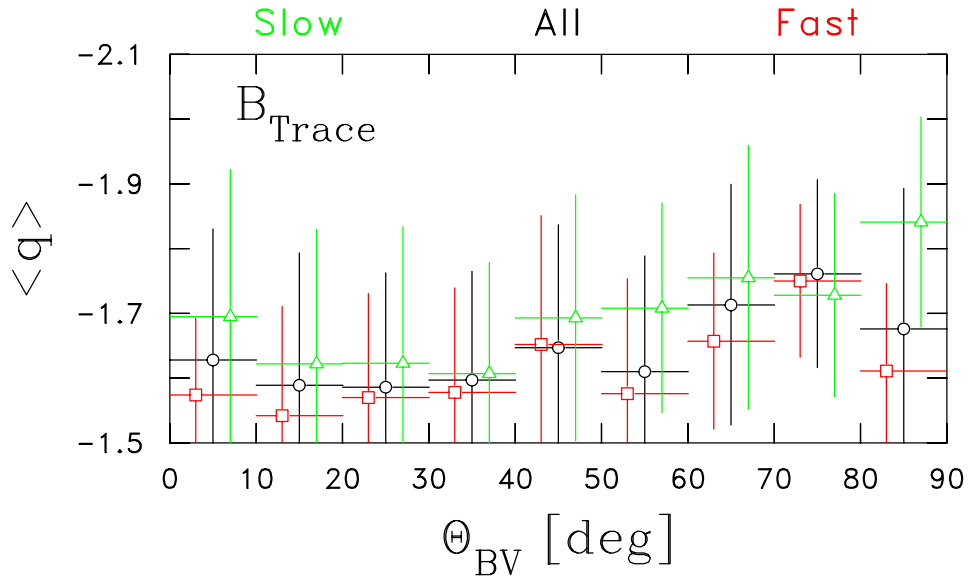


Figure 4.7: Same as top panel of Figure 4.4 except using Helios 1 magnetic field data between 0.3 and 1 AU during the years 1974 to 1976 in the frequency range 5-20 mHz.

8 mHz to 100 mHz. Note that the study of *Horbury et al.* [15] analyzed a similar frequency range, 15 mHz to 98 mHz.

Figure 4.6 shows the results of the study. The power spectrum has been computed over the specified frequency range and the indices separated into 10° bins. As before, the error bars display standard deviations; errors-of-the-mean are roughly ten times smaller than this. Also, the database is again subsetting for fast and slow wind and we add the magnetic clouds subset. $\Theta_{BR} < 30^\circ$ appears to be consistent with $-5/3$. However, $20^\circ < \Theta_{BR} < 30^\circ$ and $0^\circ < \Theta_{BR} < 10^\circ$ suffer from a lack of data points. Indeed, $10^\circ < \Theta_{BR} < 20^\circ$ is entirely absent of fast wind. In spite of this, we see in the angles $\Theta_{BR} < 30^\circ$ that there is no trend toward -2 ; if anything, there is flattening at these small angles.

4.2.3 Helios 1 MAG Data

The motivation to use Helios data is to avoid contamination by upstream waves and extend our analysis closer to the Sun where the turbulence is less evolved. This database contains 380 intervals of IMF spectra from the Helios 1 spacecraft during the years 1974-1976. The data ranges from 0.3 to 1 AU and the intervals are typically several hours. We use the same analysis here as was used in Section 4.2.2. The frequency range analyzed here is 5 to 20 mHz, the middle of the inertial range. Every effort has been made to capture the broadest possible range of solar wind conditions. Figure 4.7 shows the results of the analysis from the Helios database. We see from this plot that there is no -2 spectral index. Instead there appears to be a flattening of the spectrum associated with radial mean field conditions for $\Theta_{BR} < 40^\circ$. This may be related to the findings of *Bavassano et al.* [2] that spectral index steepens with increasing heliocentric distance. Also it is interesting to note that the fast wind is flatter than the slow wind.

4.3 Conclusions

It is unknown why the velocity appears to have the spectrum of Kraichnan [19] while the magnetic spectrum is that of Kolmogorov [18]. *Roberts et al.* argues that the velocity spectrum evolves to $-5/3$ by 5 AU [28], but this dichotomy remains unexplained at 1 AU. The study of *Tessein et al.* has found no evidence of critical balance. It does not argue that -2 spectra are unobserved; rather Figure 4.4 shows that it is present but infrequent. *Tessein et al.* [33] and *Horbury et al.* [15] can be made compatible if we postulate that different inertial range scales have different properties. As this thesis is being written, studies of the discrepancy are underway and will be investigated during the summer of 2009.

Chapter 5

Corotating Interaction Regions at 1 AU

5.1 Motivation

The results of this analysis will be compared with the turbulence parameters obtained from the Hamilton database (see Chapter 4). The key difference between this CIR study and *Hamilton et al.* is that the latter analyzes turbulence during solar maximum conditions that were taken from nominally homogenous time periods. My database contains solar minimum events and the CIR is expected to be nonhomogeneous. Since the data of *Hamilton et al.* comes from times of solar maximum we will be able to look at how the turbulence changes throughout the solar cycle. Also, since the CIR is a source region for the generation of turbulence and the database of *Hamilton et al.* studied the properties of turbulence with many distributed sources that failed to resolve source properties, this study will enable us to study the source properties and potentially separate them from the state to which the turbulence evolves. If clear distinctions are seen, then we can learn something about the source dynamics that drive turbulence. If few distinctions are seen, then it may be possible that the turbulence evolves faster than the source or possesses properties in common with the source. In addition to comparing our results with results from the Hamilton database we have also compared these CIR turbulence properties to one another and found that they are mostly identical to one another.

Figure 5.1 depicts an example of data used for this study. Leading into day 51 the spacecraft observes slow solar wind that is slowly decreasing in speed. The local IMF is directed away from the Sun ($\lambda < 90^\circ$). The density is slowly rising and the temperature is steady while alpha particle density scales with proton density and IMF fluctuations are low. At the start of day 51 the wind speed rises, density begins to rise, and IMF intensity rises, marking the start of the CIR. Over a period of ~ 12 hours the wind speed rises from 400 to 600 km/s and the density peaks. The IMF intensity peaks with the density as the magnetic field is compressed between the converging flow. By late in the day the spacecraft emerges into a high-speed wind that is hotter than its previous environment with an increased IMF intensity, marking the passage of the CIR.

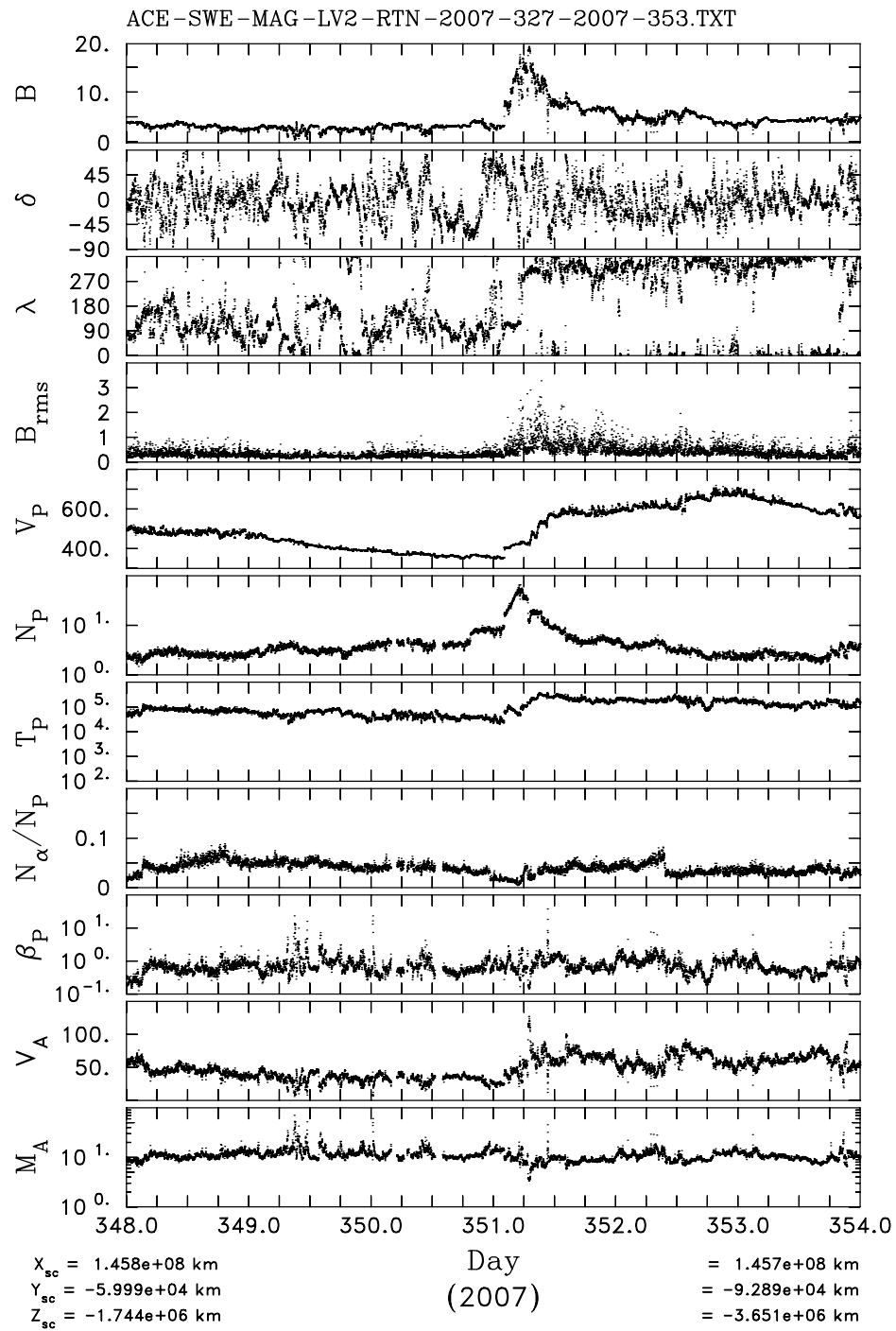


Figure 5.1: One of the CIRs used for this study. Note the standard features of a CIR: spike in magnetic field and density, and rise in wind speed and temperature.

Table 5.1: Time intervals of CIRs used in this study.

Year	CIR interval (days)	Total interval studied (days)
2007	298.25-299.0	297-299 (inclusive)
2007	316.5-318.0	316-318 (inclusive)
2007	351.0-351.5	350-352 (inclusive)
2008	58.5-60.0	56-60 (inclusive)
2008	68.25-69.75	67-70 (inclusive)

5.2 Data

The data used for this study consists of five CIR events from 2007 and 2008. Each CIR is one to two days long and we analyze the surrounding area such that the entire analyzed interval encompasses four to five days. Table 5.1 lists the time intervals studied. The data is broken down by eye into smaller intervals (around one hour) of similar activity. Of this data only intervals that produced well defined spectra were retained, but the value of the power law index was not a discriminating factor in the elimination of these intervals. The power spectra produced were manually split over two frequency intervals; the inertial range and the dissipation range. The frequency range around the spectral break was not analyzed. These two frequency intervals were fit to separate power law forms and the power law indices were recorded. An example of this fitting to separate frequencies is shown in Figure 3.2.

5.3 Results

Figure 5.2 shows two results immediately. First, the IMF fluctuation level as measured by the integrated spectrum in the top panel increases as the spacecraft passes through the CIR. Second, the inertial range power law index remains $\sim -5/3$ throughout the interval so that the rise in power is derived from a rising spectral form and not a local enhancement over a limited frequency interval as might be seen upstream of shocks. The dissipation range spectral index decreases in the fast wind when the IMF fluctuation level is highest in keeping with *Smith et al.* [31]. The inertial range slab fraction percentage seems highest before the CIR and lower in the fast wind behind. This is an unexpected result. The inertial range variance anisotropy A is modest throughout the interval. There is no magnetic helicity in the inertial range (as expected) and very little in the dissipation range.

There are key differences between the database used for this analysis and the one used for the analyses we are comparing to, *Smith et al. and Hamilton et al. 2008* [14, 31, 32]. The three previous papers use solar maximum data, while the CIR analysis is during solar minimum. The main difference we expect from the solar cycle is the fundamental difference in solar wind speed. Note that the CIR has two distinct solar wind populations: high speed winds and low speed winds (Figure 5.3). This is because of the structure of a CIR; fast wind crashing into low speed wind and an interface region marking the transition from one to another. The *Hamilton et al.* wind speed distribution is not separated, which is typical of solar maximum conditions (Figure 5.4)[14].

Another difference is geometry. The three publications being compared to the CIR represent ambient turbulence. This means that the turbulence doesn't come from one place in

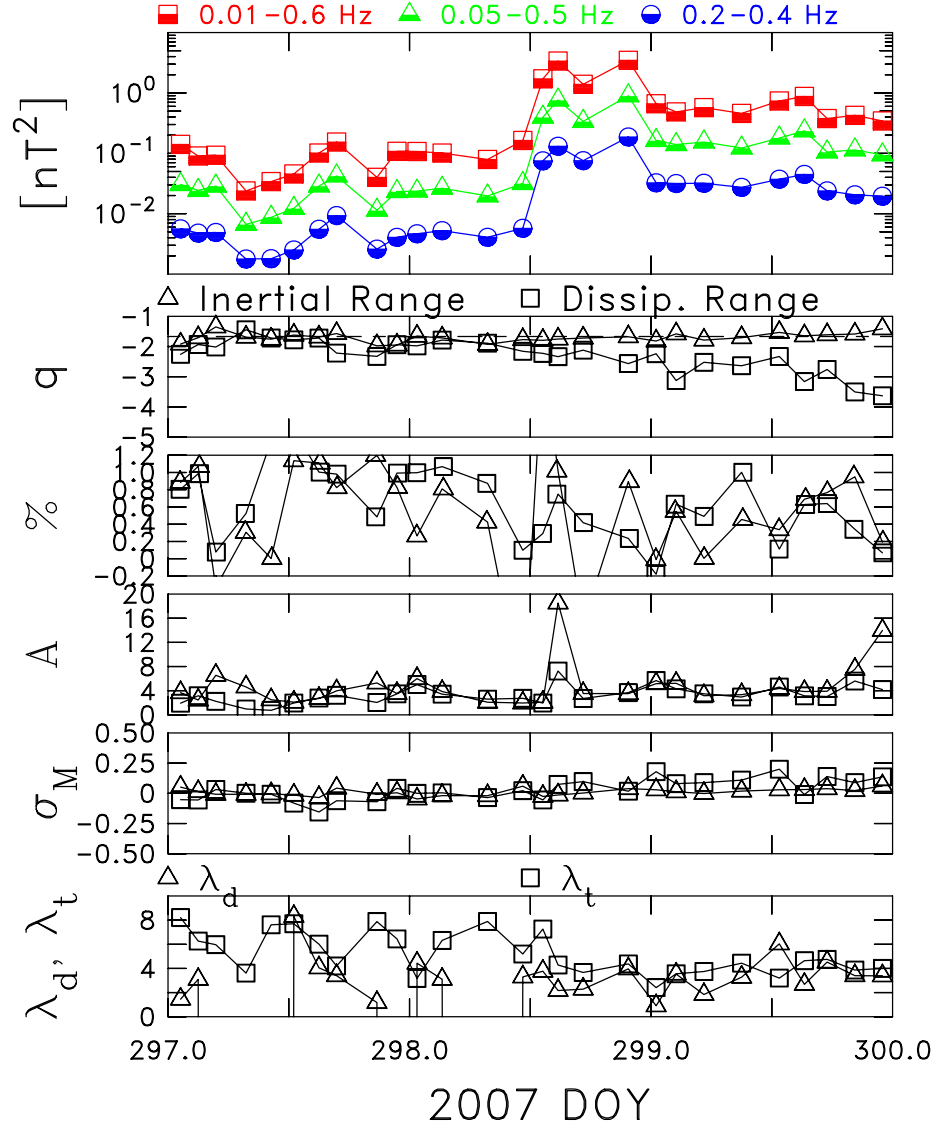


Figure 5.2: Summary of a CIR showing typical results of all five CIRs studied. Explanation of panels from top to bottom: Magnetic power, spectral index, slab percentage, anisotropy and magnetic helicity. λ_d marks the measured spatial scale for the onset of dissipation and λ_t marks the measured Taylor scale (not discussed in this paper).

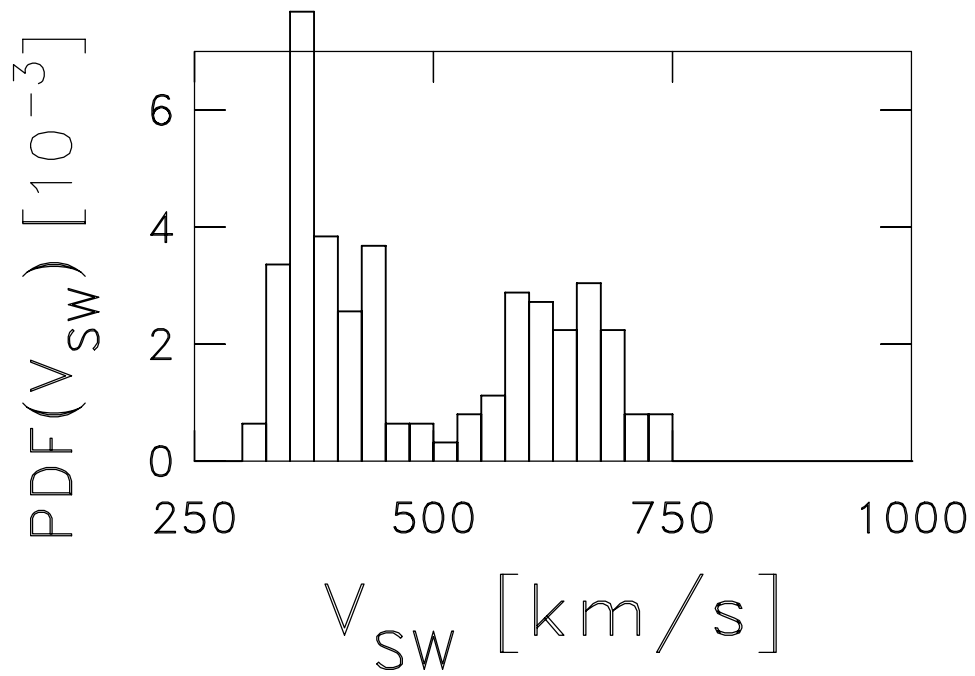


Figure 5.3: Distribution of solar wind speeds for the CIR analysis.

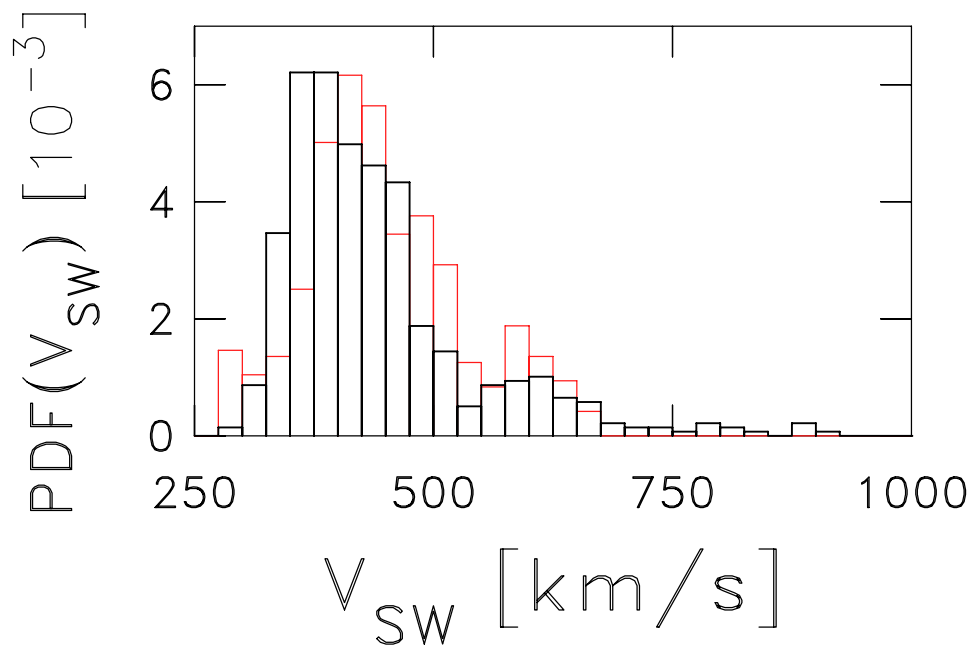


Figure 5.4: Distribution of solar wind speeds from *Hamilton et al.* [14].

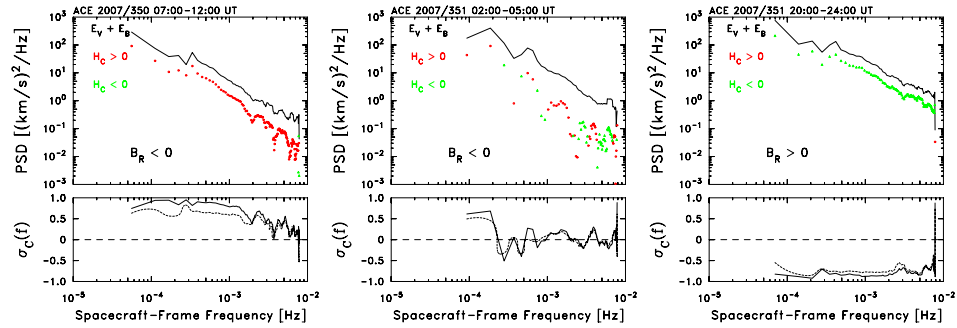


Figure 5.5: Before, during and after the CIR. Outward propagation before and after, but a mixture of both during the actual event.

particular and is well developed by 1 AU. The CIR turbulence comes from a point source (the CIR itself) and as a result, might not be isotropic and is expected to be isolated within the source region.

Figure 5.5 shows three panels from before, during, and after the CIR respectively. Each panel shows the energy, cross helicity H_C and sign of the radial magnetic field B_R , properties which together indicate the dominant propagation direction. If H_C and B_R are of opposite signs, then dominant Alfvén wave propagation is outward. If they are of the same sign then propagation is inward. We see that propagation is outward (as shown by *Belcher & Davis* [3]) before and after the CIR but there is a mixture of both during the actual event. This is something not seen in ambient turbulence, and the only difference we found between the CIR turbulence and ambient turbulence during this study. However, this difference is important as it indicates local generation of fluctuation energy by means of the flow gradient. Any smaller scale turbulence within the region is expected to result from the turbulent cascade of this newly injected energy. It is important to note that Figure 5.5 depicts larger scales than those we now examine.

Another comparison we can make between CIR turbulence and ambient turbulence is the correlation between cascade rate and spectral index. Figure 5.6 shows this distribution. We see that they are correlated in both CIR and ambient (Figure 3.10) turbulence.

We proceed to present further comparisons between CIR turbulence and ambient turbulence that yielded similar results. The *Kolmogorov* prediction that the spatial scale V_{SW}/ν_{bf} is correlated to the rate of energy cascade [18] has been shown by *Smith et al.* not to apply to the solar wind [31]. We find the same result in the CIR, that there is no correlation between these two values (See Figure 5.7).

Figure 5.8 shows the panel that is analogous to Figure 4 from *Smith et al.* [32]. In each of the plots we have good agreement with the results of *Smith et al.*. In plot (e), where *Smith et al.* finds no correlation between variance anisotropy and cascade rate, we also find no correlation in the CIR.

Variance anisotropy was looked at in this study in the same manner as in *Smith et al.* [32] and *Hamilton et al.* [14]. The distribution of variance anisotropy for the CIR turbulence is shown in Figure 5.9. This appears to be about the same as the ambient turbulence result (Figure 3.6). In both figures the distinct peak at low anisotropy is present.

Figure 5.10 is analogous to Figure 8 from *Hamilton et al. 2008* [14]. Solid lines represent Hamilton’s trend lines for magnetic clouds and open field lines in the inertial range. Dashed lines represent Hamilton’s dissipation range trend and the scatter represents CIR data. Note

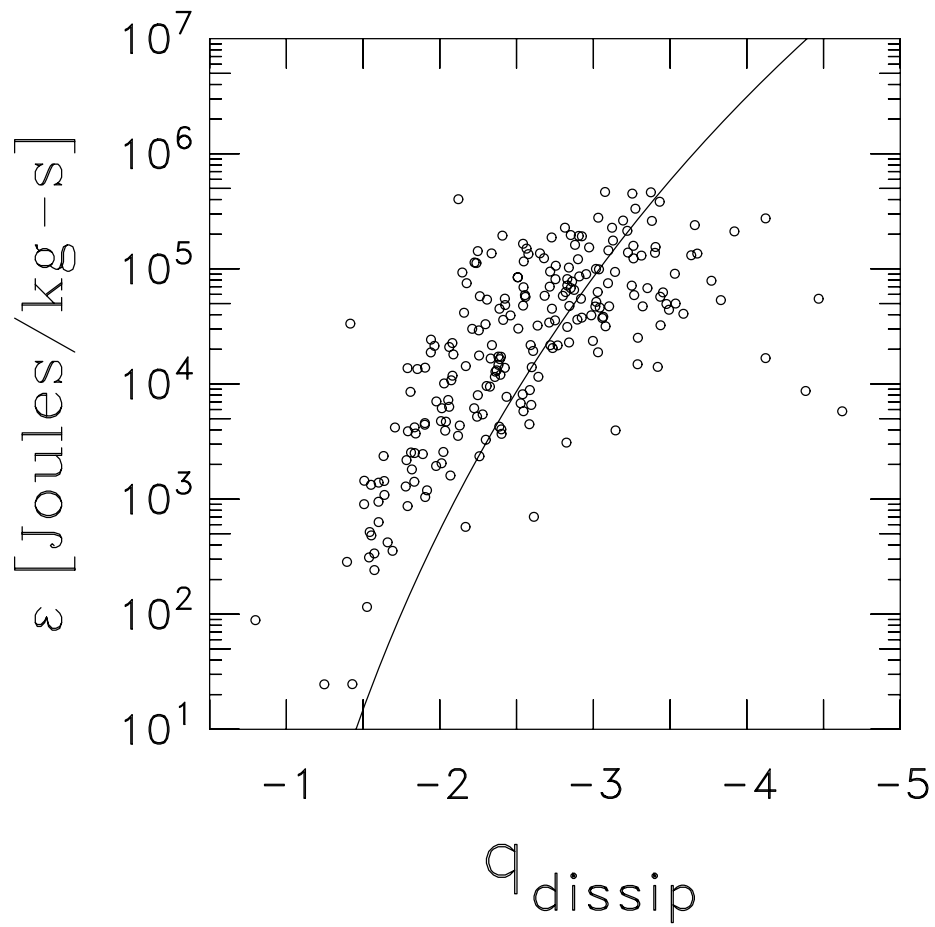


Figure 5.6: Cascade rate vs. spectral index in the dissipation range for CIR turbulence. The trend line is the fit from *Smith et al.*[31].

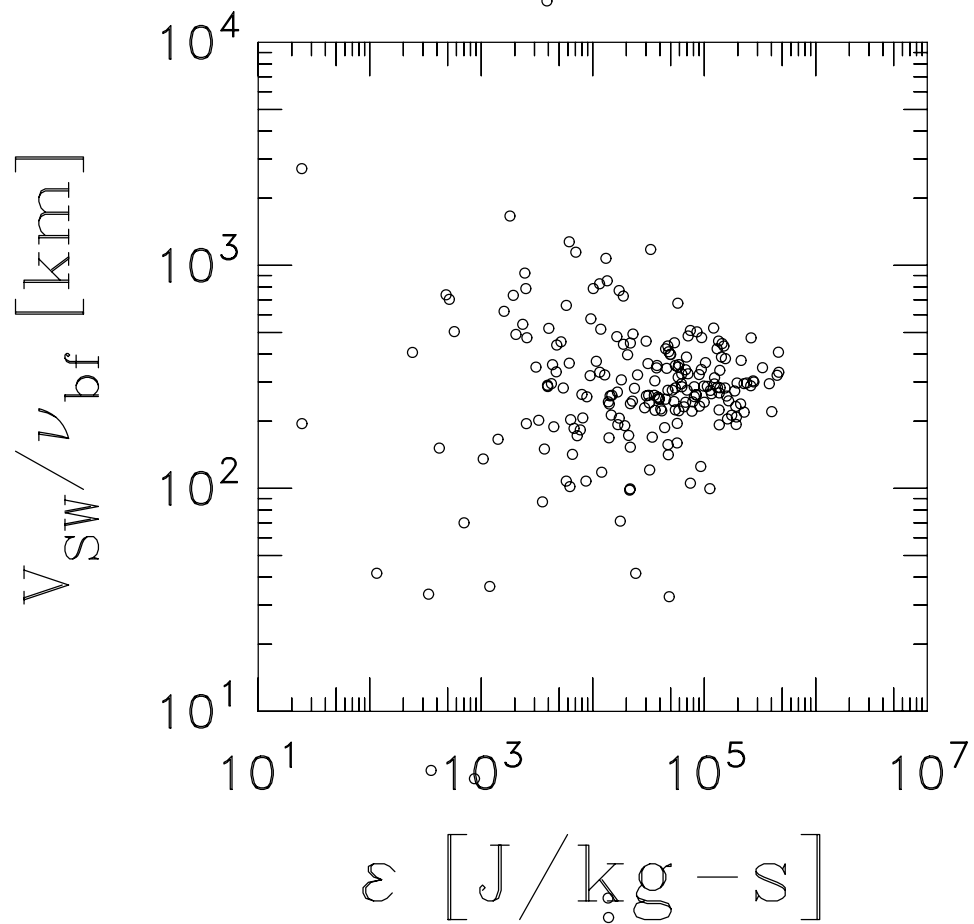


Figure 5.7: There is no correlation between cascade rate and characteristic spatial scale, contrary to the predictions of traditional hydrodynamics. This result found for the CIR is the same as the result found for ambient turbulence [31].

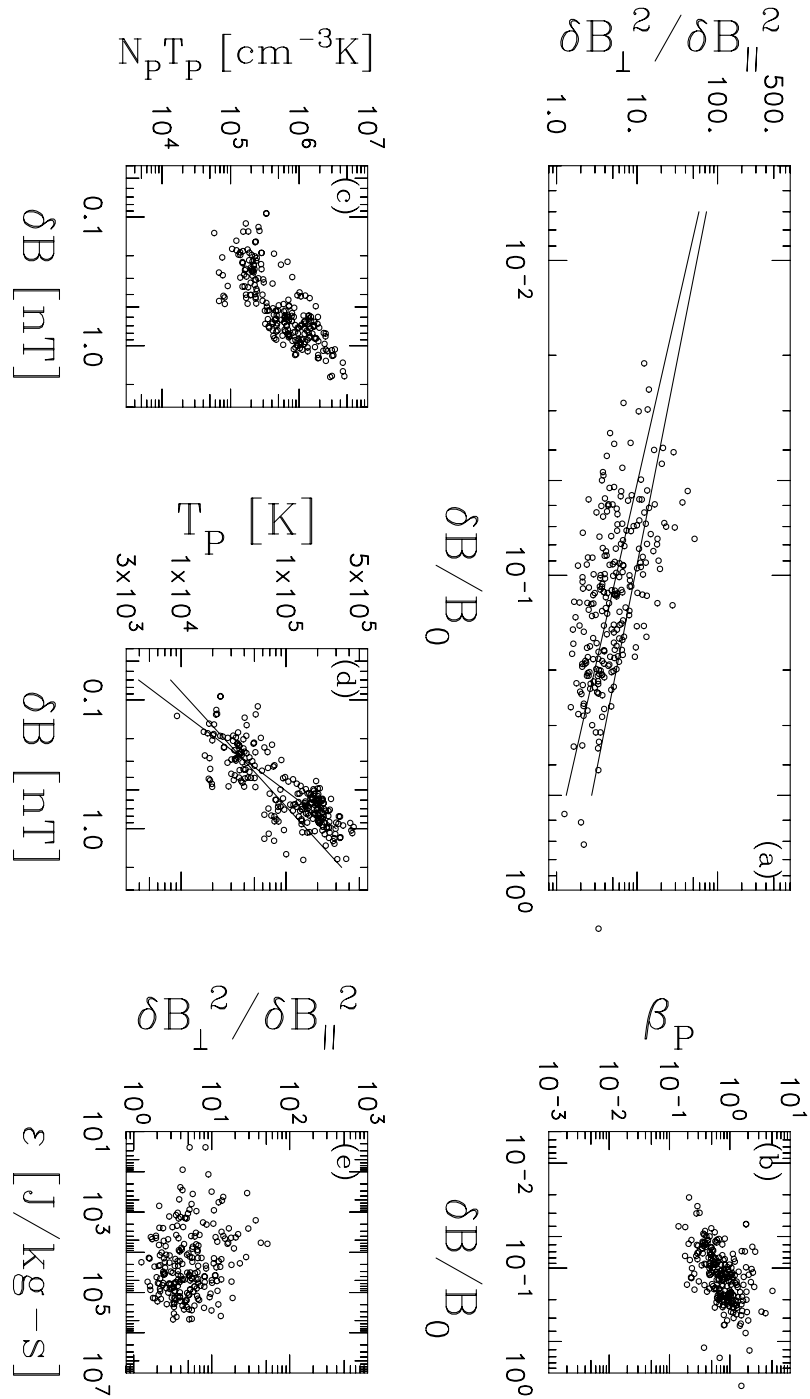


Figure 5.8: In all plots, trend lines represent a fit to the analysis of *Smith et al. 2006b* [32]. There are two lines because the analysis was subsetted for magnetic clouds and open field lines. (a) Variance anisotropy vs. $\delta B/B_0$. (b) β_P vs. $\delta B/B_0$. This shows correlation between seemingly unrelated quantities. (c) $N_P T_P$ vs. δB showing correlation between quantities not casually connected. (d) T_P vs. δB . (e) Plot of variance anisotropy vs. cascade rate ϵ . This shows that variance anisotropy is not well correlated to the rate of energy cascade.

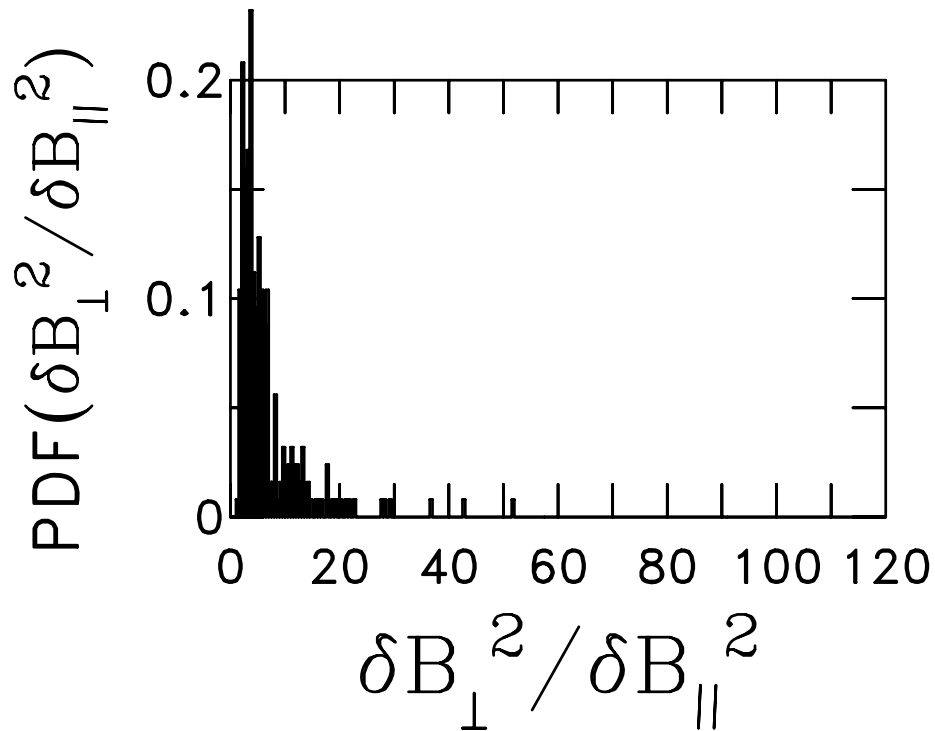


Figure 5.9: Variance anisotropy distribution function for CIR turbulence.

that neither population fits the trend lines perfectly, but the dissipation range is more similar to Hamilton than the inertial range.

In the ambient turbulence publications, it was found from comparing variance anisotropy in the inertial range to the dissipation range that the dissipation range is slightly more compressive (See Figure 3.7). Figure 5.11 shows that this is the same for CIR turbulence.

Recall the discussion of the correlation between magnetic helicity in the dissipation range and cross helicity in the inertial range (See Section 3.8). *Hamilton et al.* found that $\sigma_c/\sigma_M = -2.4$ (Figure 3.9). The result for CIR turbulence is shown in Figure 5.12. The line is $\sigma_c/\sigma_M = -2.4$ and matches the CIR data very well.

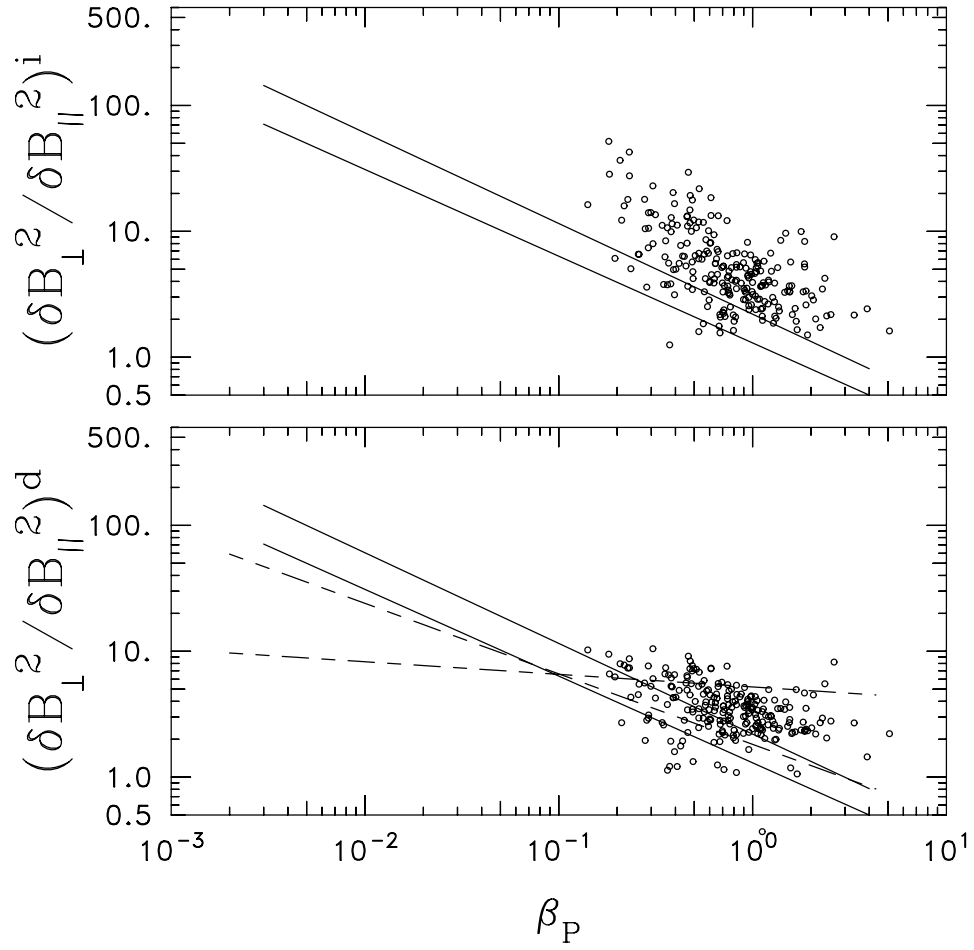


Figure 5.10: Variance anisotropy plotted against β_P for the inertial and dissipation ranges. The trend line is the *Smith et al.* result [32].

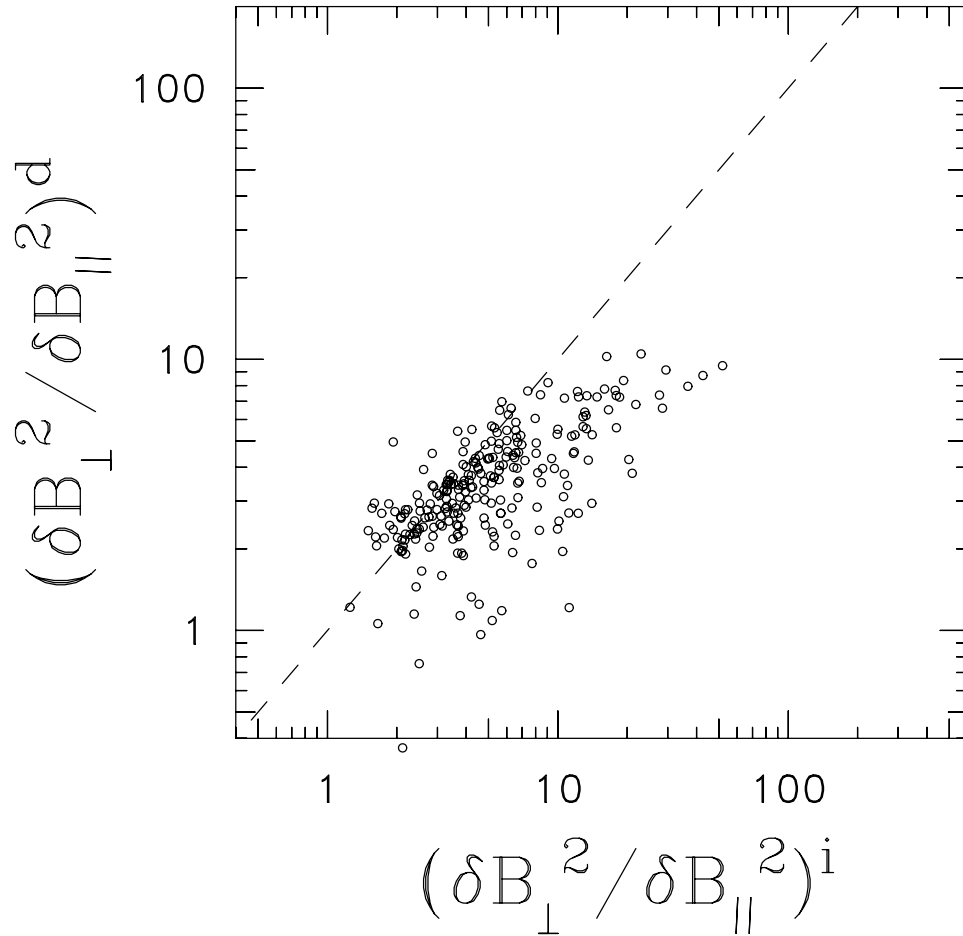


Figure 5.11: Correlation for variance anisotropy between the inertial range and dissipation range.

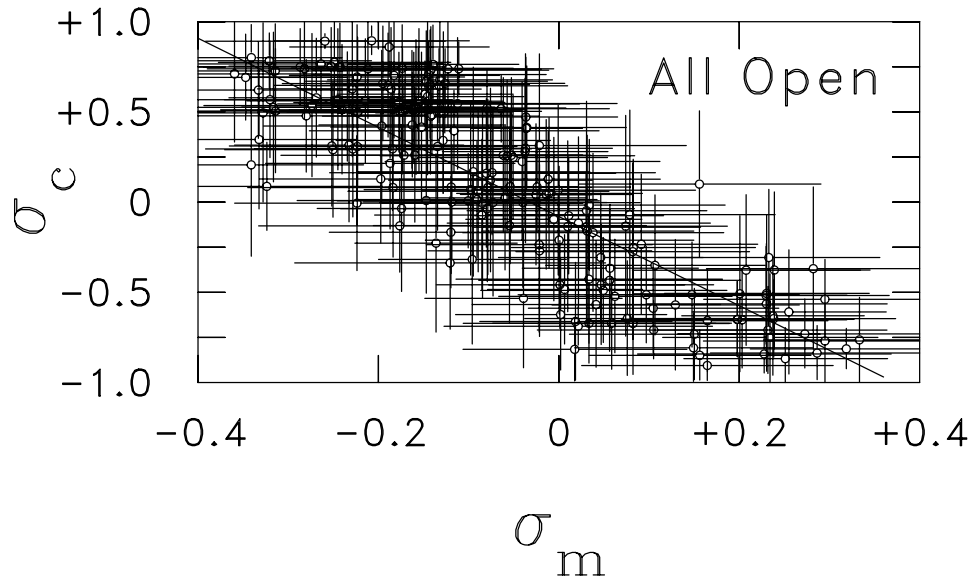


Figure 5.12: Correlation between magnetic helicity in the dissipation range vs. cross helicity in the inertial range for CIR turbulence (with error bars). $\sigma_c/\sigma_M = -2.4$, the same result as *Hamilton et al.* [14].

Chapter 6

Discussion

We have found from the results of analyses discussed in Chapters 4 and 5 that scale seems to be an important factor in the study of plasma waves in interplanetary turbulence. Recall the unresolved disagreement between *Tessein et al.* [33] and *Horbury et al.* [15], which seems to have arisen from their analysis of different scales. The matter has cropped up again in the CIR study because at small scales CIR turbulence is the same as ambient turbulence, but there is a clear difference at large scales. We may be able to explain this in terms of eddy lifetimes.

We see from Figure 6.1 that the eddy lifetime is shorter at smaller scales. Since turbulence evolves on the scale of an eddy lifetime, a length scale that contains many lifetimes may be fully evolved while a scale with fewer lifetimes may not be. This means that small scales are representative of universal trends while large scales show only local properties. This makes sense in the case of the CIR because we found common properties between the CIR and ambient turbulence at small scales, but differences at larger scales. As the energy is cascading from large scale to small scale in the CIR the turbulence is evolving such that it matches properties found in the ambient turbulence.

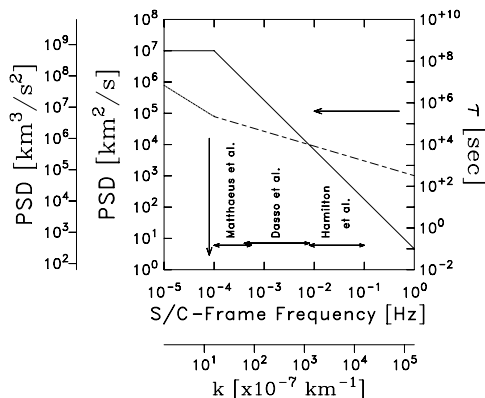


Figure 6.1: Plot of power spectrum (solid) and eddy lifetime (dashed). The time for a parcel to travel 1 AU is marked by the arrow. [14]

Bibliography

- [1] Alfvén, H., Existence of electromagnetic-hydrodynamic waves, *Nature*, *150*, 405-406, 1942.
- [2] Bavassano, B., M. Dobrowolny, F. Mariani, and N. F. Ness, Radial evolution of power spectra of interplanetary Alfvénic turbulence, *J. Geophys. Res.*, *87*, 3617–3622, 1982.
- [3] Belcher, J. W., and L. Davis, Jr., Large-amplitude Alfvén waves in the interplanetary medium, *J. Geophys. Res.*, *76*, 3534–3563, 1971.
- [4] Bieber, J. W., W. Wanner, and W. H. Matthaeus, Dominant 2D magnetic turbulence in the solar wind, *Solar Wind Eight*, edited by D. Winterhalter, J. Gosling, S. Habbal, W. Kurth and M. Neugebauer, AIP Conference Proceedings 382, 355–357, 1996.
- [5] Borovsky, J. E. (2008), Flux tube texture of the solar wind: Strands of the magnetic carpet at 1 AU?, *J. Geophys. Res.*, *113*, A08110, doi:10.1029/2007JA012684.
- [6] Burlaga, L. F., and K. W. Behannon, Magnetic clouds: Voyager observations between 2 and 4 AU, *Sol. Phys*, *81*, 181, 1982.
- [7] Burlaga, L. F., McDonald, F. B., Ness, N. F., Schwenn, R., Lazarus, A. J., & Mariani, F. 1983, NASA STI/Recon Technical Report N, 84, 18149
- [8] Coleman, P. J., Jr., Hydromagnetic waves in the interplanetary plasma, *Phys. Rev. Lett.*, *17*, 207–211, 1966.
- [9] Coleman, P. J., Jr., Turbulence, viscosity, and dissipation in the solar wind plasma, *Astrophys. J.*, *153*, 371–388, 1968.
- [10] Dasso, S., L. J. Milano, W. H. Matthaeus, and C. W. Smith, Anisotropy in Fast and Slow Solar Wind Fluctuations, *Astrophysical Journal Letters*, *635*, L181–L184, 2005.
- [11] Formisano, V. and C. F. Kennel, Small amplitude waves in high β plasmas, *J. Plasma Phys.*, *3*, 55–74, 1969
- [12] Goldreich, P., and S. Sridhar, Toward a theory of interstellar turbulence. II. Strong Alfvénic turbulence, *Astrophys. J.*, *438*, 763–775, 1995.
- [13] Gosling, J. T., and V. J. Pizzo, Formation and evolution of corotating interaction regions and their three dimensional structure, *Sp. Sci. Rev.*, *89*, 21–52, 1999.
- [14] Hamilton, K., C. W. Smith, B. J. Vasquez, and R. J. Leamon, Anisotropies and Helicities in the Solar Wind Inertial and Dissipation Ranges at 1 AU, *Journal of Geophysical Research*, *113*, A01106, doi:10.1029/2007JA012559 (2008).

- [15] Horbury, T., M. Forman, and S. Oughton, Measurements of the wavevector anisotropy of solar wind turbulence, *Eos Transactions, American Geophysical Union*, 88(52), Fall Meeting Supplement, Abstract SH33B-02, 2007.
- [16] Hundhausen, A. J., *Solar Wind and Coronal Expansion*, Physics and Chemistry in Space Vol. 5, edited by J. G. Roederer, Springer-Verlag, New York, 1972.
- [17] Kallenrode, M.-B., *Space Physics*, Springer-Verlag, New York, 2001.
- [18] Kolmogorov, A. N., The local structure of turbulence in incompressible viscous fluid for very large Reynolds numbers, *Dokl. Akad. Nauk SSSR*, 30, 301–305, 1941. (Reprinted in *Proc. R. Soc. London A*, 434, 9–13, 1991.)
- [19] Kraichnan, R. H., Inertial range of hydromagnetic turbulence, *Phys. Fluids*, 8, 1385–1387, 1965.
- [20] Leamon, R. J., C. W. Smith, N. F. Ness, W. H. Matthaeus, and H. K. Wong, Observational constraints on the dynamics of the interplanetary magnetic field dissipation range, *J. Geophys. Res.*, 103, 4775–4787, 1998.
- [21] Leamon, R. J., W. H. Matthaeus, C. W. Smith, and H. K. Wong, Contribution of cyclotron-resonant damping to kinetic dissipation of interplanetary turbulence, *Astrophys. J. Lett.*, 507, L181-L184, 1998.
- [22] McComas, D. J., H. A. Elliott, N. A. Schwadron, J. T. Gosling, R. M. Skoug, and B. E. Goldstein, The three-dimensional solar wind around solar maximum, *Geophys. Res. Lett.*, 30(10), 1517, doi:10.1029/2003GL017136, 2003.
- [23] Matthaeus, W. H. and M. L. Goldstein, Measurement of the rugged invariants of magnetohydrodynamic turbulence in the solar wind, *J. Geophys. Res.*, 87, 6011–6028, 1982.
- [24] Matthaeus, W. H., M. L. Goldstein, and D. A. Roberts, Evidence for the presence of quasi-two-dimensional nearly incompressible fluctuations in the solar wind, *J. Geophys. Res.*, 95, 20,673–20,683, 1990.
- [25] Parker, E. N., Dynamics of the interplanetary gas and magnetic fields, *Astrophys. J.*, 128, 664–676, 1958.
- [26] Parker, E. N., *Interplanetary Dynamical Processes*, Wiley-Interscience, New York, 1963.
- [27] Podesta, J. J., D. A. Roberts, and M. L. Goldstein, Power spectrum of small-scale turbulent velocity fluctuations in the solar wind, *J. Geophys. Res.*, 111, A10109, doi:10.1029/2006JA011834, 2006.
- [28] Roberts, D. A., *Eos Transactions, American Geophysical Union*, 88(52), Fall Meeting Supplement, Abstract SH31B-06, 2007.
- [29] Simunac, K., *Solar Wind Stream Interfaces: The Importance of Time, Longitude, and Latitude Separation Between Points of Observation*, University of New Hampshire, Durham (New Hampshire), 2009.

- [30] Smith, C. W., W. H. Matthaeus, and N. F. Ness Measurement of the Dissipation Range Spectrum of Magnetic Fluctuations in the Solar Wind with Applications to the Diffusion of Cosmic Rays, *Proceedings of the 21st International Cosmic Ray Conference* (Adelaide), **5**,280-283 (1990)
- [31] Smith, C. W., K. Hamilton, B. J. Vasquez, and R. J. Leamon, Dependence of the dissipation range spectrum of interplanetary magnetic fluctuations upon the rate of energy cascade, *Astrophys. J. Lett.*, *645*, L85-L88, 2006.
- [32] Smith, C. W., B. J. Vasquez, and K. Hamilton, Interplanetary magnetic fluctuation anisotropy in the inertial range, *J. Geophys. Res.*, *111*, A09111, doi:10.1029/2006JA011651, 2006.
- [33] Tessein, J. A., C. W. Smith, B. T. MacBride, W. H. Matthaeus, M. A. Forman, J. E. Borovsky, Spectral indices for multi-dimensional interplanetary turbulence at 1 AU, *Astrophys. J.*, *692*, 684–693, 2009.